THE USE OF STRESS TRAJECTORY IN PREDICTING FRACTURE PROPAGATION PATH AROUND INJECTOR AND PRODUCER WELLS

by

Ayodeji Owowa

Submitted in partial fulfillment of the requirements

for the degree of Master of Applied Science

at

Dalhousie University

Halifax, Nova Scotia

August 2023

Dalhousie University is located in Mi'kma'ki, the ancestral and unceded territory of the Mi'kmaq.

We are all Treaty people.

Contents

List of Figures

Abstract

It is well documented both in the field and in laboratory experiments that hydraulic fracture could deviate from its original plane of propagation, typically parallel to the direction of the maximum principal stress, due to varying stress and pore pressure conditions. It has also been observed that due to possible stress reversal around a previously fractured well, refracturing a well may lead to new fractures, orthogonal to the original fracture.

This work considered two problems. First, the possible path of propagation of a fracture in the neighborhood of unfractured fluid injector-producer pair using the stress trajectory concept was re-examined. A fracture initially equidistant between the wells was shown to likely propagate in the direction of the injection well as indicated by the maximum principal stress trajectories around the fracture-well system, provided a particular dimensionless fracture toughness is small. Additional parameters such as the far field stress deviator and the production/injection times were shown to have significant impact on the stress field perturbation. A modified stress trajectory equation that incorporate fracture toughness effect in order to approximate the fracture propagation direction was also introduced.

The second problem examined the stress reorientation around an unpropped fractured producer. The extent of the orthogonal segment of the refracture half-length as a function of production time and far-field stress deviator for a purely poroelastic case as well as the relevant parameters influencing the extent of stress reversal around the fractured well was examined. Adequate knowledge of the stress field will be quite helpful in future re-development of existing fields with fractured wells.

List of Abbreviations and Symbols Used

BEM	Boundary Element Method
DDM	Displacement Discontinuity Method
KGD	Khristianovic and Geertsma and de Klerk
PKN	Perkins and Kern and Nordgren
c	diffusivity coefficient
B	Skempton's pore pressure coefficient
E	Young's Modulus
$Ei(x)$	exponential integral
F_k	point force source in the k direction
$\digamma_u$	dimensionless stress difference
$\digamma_{ij}$	stress functions
g	fluid leak-in rate
G	shear modulus
k	intrinsic permeability
k_u	permeability coefficient
K	drained bulk modulus
K_u	undrained bulk modulus
K_o	modified Bessel function of the second kind
l_r	dimensionless orthogonal segment of the theoretical refracture half length
L	fracture half-length
M	Biot Modulus
p	pore pressure
p_o	initial pore pressure
P_o	far field mean stress
q_i	fluid flux per unit length
Q_o	fluid flowrate per unit length
r	radial distance
s	Laplace transform parameter
S	uniaxial specific storage coefficient
S_o	far field deviatoric stress
t	real time

u_r	radial displacement
u_θ	tangential displacement
v	Poisson ratio, drained
v_u	Poisson ratio, undrained
$\mathbf{x}$	2D dimensional coordinate of a field point
α	Biot coefficient
δ_{ij}	Kronecker delta
ε	volumetric strain
ε_{ij}	solid strain tensor
η	poroelastic stress constant
ζ	variation in fluid content per unit reference volume
τ	dimensionless time
μ	dynamic viscosity of fluid
ϑ	dimensionless toughness fitting parameter
χ	dimensionless toughness parameter
Υ	dimensionless toughness parameter modifier
θ_p	angle the principal stress makes with the positive $x-axis$
$\Phi(\tau)$	normalized cumulative leak-in volume
$\psi^*(x,\tau)$	fluid source density in time domain
$\tilde{\psi^*}(x,s)$	fluid source density in Laplace space
$\psi(x',\tau')$	dimensionless leak-in rate
$\psi(x',s)$	Laplace image of the dimensionless leak in rate
γ	source density
σ_{ij}	total stress tensor
σ_{ij}^{ind}	actual induced stress components
σ_{ij}^{aux}	induced stress components to auxiliary problem
$\mathcal{S}$	dimensionless far-field deviatoric stress
Π	dimensionless fluid pressure
$\hat{\Pi}(s)$	Laplace image of dimensionless fluid pressure

Acknowledgments

I would like to start by expressing my deepest gratitude to my advisor Dr. Dmitry Garagash for his painstaking guidance, kindness and inestimable support during my studies at Dalhousie University. His thoughtfulness and genuine support all through my various struggles was a great motivation to finish the program. Thank you for not giving up on me.

I would also like to appreciate my supervisory committee, Dr. Farid Taheri and Dr. Andrew Corkum for their support and willingness to accommodate my short notices and quite frankly unreasonable expectations. Yet they stood by me and helped me to the finish line. Thank you for your sacrifice.

I am very grateful to my family for being such a great support, my wife, Blessing and my two boys Daniel and Emmanuel for their sacrifice and understanding, my parents and elder brother, Engr. Rotimi Owowa for their continual encouragement to stay the course and complete the program. Thank you for your support all through the difficult times.

Finally, I want to thank the Almighty God and my Lord Jesus Christ for strength and grace to complete this program, without which, it would have been impossible.

The financial support of the Natural Science and Engineering Research Council of Canada is deeply appreciated.

Chapter 1

Introduction

1.1 Background

Hydraulic fracturing (HF) also commonly known as fracking plays a significant role in the production of hydrocarbons from conventional and unconventional reservoirs. Unconventional hydrocarbon reservoirs (tight gas, tight oil and shale formations) that were once considered uneconomical or cap rocks due to their low porosity and permeability can now be developed economically with hydraulic fracturing. The "shale boom" is a testament to the success of the hydraulic fracturing technology. Hydraulic fracturing, however, do have other use cases apart from hydrocarbon extraction. This includes underground waste drill cuttings disposals, measurement of in-situ stresses and heat production from geothermal reservoirs.

Hydraulic fracturing generally involves injecting high-pressured fluid into a confined section of a borehole until a fracture is initiated due to tensile failure of the rock in the pressurized section. Depending on the objective of the fracturing process, additional fluid may be injected to propagate the fracture and proppants may be introduced to keep the fracture open. This is usually the case for hydrocarbon stimulation which will be of primary concern in this thesis.

Hydrocarbon stimulation hydraulic fracturing is a multi-stage well stimulation technique [27]. The first stage (also called "the pad") involves injecting only fluid (usually water) at high pressures through the wellbore into the target segment of the reservoir to create a fracture. A fracture is initiated when the injected fluid pressure exceeds the minimum confining stress of the reservoir. The second stage involves the injection of a slurry, a mixture of water, some additives and propping agents such as graded sand and ceramics. The purpose of the proppants is to keep the created fracture open and provide pathways for the reservoir fluids to flow towards the wellbore. This second stage treatment is often carried out multiple times till the desired proppant concentration are placed in the fractures. The third stage, also called the flush stage

involves pumping fluid only down the wellbore to help breakdown some gel deposits and clean up stranded proppants from the wellbore. The well is shut in for a while to allow all the pumped fluid to be lost to the formation while also allowing the fracture to close on to the proppants properly before the well is then put to production.

While hydraulic fracturing started with vertical wells, the technique has been extended to horizontal wells and has found great success in several unconventional reservoir formations such as Bakken, Barnett, Eagle ford and Marcellus shales to name a few [13]. The hydraulic fracturing conducted in horizontal wells are usually completed on various segments of the well (often referred to as stages). The number of perforation clusters or stages on a well is dependent on the lateral length of the well.

The "plug and perf" method is the most commonly used approach of completing multi-stage hydraulic fracturing in horizontal wells. The method involves running an assembly of perforation guns and frac plugs on a wireline or coiled tubing into the well to perforate the desired sections of the well so that fracturing fluid can be pumped down to fracture the target section. Once the first stage or section (usually near the toe of the well) is fractured, perforating guns and plugs are run on a wireline again into the well to seal off the first stage with the plug before the second stage or segment is perforated and fractured. The process is repeated till the entire length of interest is perforated and fractured. The plugs are then milled out with a drill bit on a coiled tubing before putting the well to production.

Oftentimes, the initial stimulation implemented for an unconventional reservoir may not adequately recover the hydrocarbon reserve in the formation. This could be due to a number of different factors such as poor initial well design and completion. To access the unrecovered hydrocarbons, operators generally explore two main options: drill new infill wells or refracture existing wells. The decision as to which approach to adopt is dependent on various factors including the reservoir characteristics, the existing field development plan, the current stress regime and the economics around each strategy among many other variables [58].

1.2 Refracturing in Oil and Gas Fields

Refracturing (or refracking) is a well restimulation technique with a primary objective of improving the production rates from existing fractured wells with declining production. The decline in production rates may be due to lost fracture conductivity caused by proppant embedment and degradation, cyclic stress, gel damage and fines plugging among other factors [58]. Refracturing helps with reopening and extending existing fractures which restores or improves fracture conductivity. Other benefits include creating new fractures to contact virgin segments of the reservoir due to the reorientation of the stress fields and re-energizing natural fractures. When

the goal is to contact new segments of the reservoir between existing perforations, isolation packers and seal assemblies on a coiled tubing are used to isolate existing perforation clusters and restimulate the target intervals [58]. A more recent approach is to use refrac liners specifically designed to isolate the entire sections of the old perforations with enough internal diameter to accommodate perforation guns, plugs and fluid and proppant pumping at high rates[38].

A major attraction of refracturing over drilling in-fill wells is cost. Refracturing costs a fraction of new wells [37]. A refracture could costs between $1 million to $3 million while a brand new well may cost anywhere between $8 million and $16 million depending on depth, location and type among other factors.

This thesis is devoted towards understanding the stress regime around existing production and injection wells with the goal of providing some guidelines for the hydraulic fracture designer who is considering refracturing existing wells.

1.3 Objectives of the Study

While hydraulic fracturing (HF) has been around for well over 50 years, the technique is far from being perfected and has remained a major research focus in the oil and gas industry. HF modeling is a science in its own class with myriads of factors that must be considered in order to have an effective design. One area of ongoing research in HF modeling is understanding how stress perturbation due to fluid injection or pumping would influence the direction of fracture propagation in a porous media especially during a refracturing operation [7, 45, 13].

The objective of the thesis is to examine the stress state around injection and production wells due to injection and pumping activities, within a 2D plane strain model. Of particular interest is to study the influence of the induced stress field evolution on the possible path a fracture will follow using the concept of stress trajectories. Two problems were studied. First is the Berchenko-Detournay Problem in which a fracture was initially at a location equidistant from an unfractured injector-producer pair injecting and pumping fluid at a constant rate. The second problem pertains to a single fractured producer well being considered for a refracturing operation.

To accomplish the set objective, the following methodology was adopted.

For the first problem, the stress field equations around the wells were first derived from the governing equations of poroelasticity following previous work done by Berchenko and Detournay [7]. The obtained induced stresses were then used to construct the stress trajectories around the fracture-well system. For the second problem, the stress field equations were formulated using the poroelastic stress fundamental solutions of a point source and the transient pressure solutions developed by Sarvaramini and Garagash[47]. Where applicable, asymptotic solutions

were also reported to help validate numerical solutions. The solution for the second problem were sought in Laplace space before being inverted back to the time domain. Stress trajectories were used to map the likely fracture growth path. Dimensionless groups were also used to simply derivations and generalize the formulations in both problems. Solution to the formulations were implemented using the computer software, Mathematica.

It should be noted that actual fracture propagation was not modeled in this work, but rather the possible path a propagating fracture may follow due to poroelastic induced stresses were examined. Also, the study was carried out within the poroelastic framework which adequately describes the behaviour of a solid medium under some loading when saturated with fluid, for which an hydrocarbon reservoir is an excellent example .

An understanding of the perturbed stress field must be put into consideration when planning a refracturing operation as it is expected to have non-trivial effects on the refracturing requirements as well as the refracture characteristics (direction, length and interaction with neighboring cracks).

1.4 Organization of the Thesis

This thesis is organized as follows:

Chapter 1 provides a general background introduction to HF, refracturing and research objectives.

Chapter 2 provides a review of existing literature on the HF and refracturing techniques as well as the concept of stress reorientation.

Chapter 3 provides some details on the mathematical framework and equations on poroelasticity to model the stress state in a poroelastic medium as well as the numerical solution techniques adopted in the work.

Chapter 4 covers stress field re-orientation in a single unfractured injector-producer system. Attraction and repulsion zones around the injection and producer wells are examined. A heuristic semi-analytical approach is also developed to predict the path of a propagating fracture as it approaches an injector. This is done as an alternative to full scale numerical modeling to predict the fracture path.

Chapter 5 examines stress reorientation around a fractured producer that is being considered for refracturing. The influence of the difference between the induced horizontal stresses on the stress-reversal envelop around the wells are also examined. An asymptote for the stress difference is also established for extended production times.

Chapter 6 closes out the thesis with conclusions and recommendations for further research.

Chapter 2

Literature Review

2.1 Introduction

In tectonically relaxed reservoirs, characterized by normal faults, the general state of stress is such that the three orthogonal principal stresses - the vertical overburden stress, the principal maximum horizontal stress and the principal minimum horizontal stress are not equal [35, 27] . In shallow reservoirs (<2000 ft deep), the smallest of these three stresses is the overburden stress and as such fractures are expected to be horizontal since hydraulic fracture propagate in the direction perpendicular to the direction of the minimum confining stress. In deep reservoirs (> 2000 ft), hydraulic fractures would propagate in the direction perpendicular to the direction of the principal minimum horizontal stress because it is the least of the three principal stresses and as such vertical fractures are expected to be created. Deep reservoirs and by extension vertical fractures are the most prevalent in practice.

2.2 Hydraulic Fracture Models

One important consideration in the design of hydraulic fractures is the fracture geometry which is a function of lithological and related stress heterogeneity of the reservoir conditions, fracture pressure, injection rates, fracturing fluid type and proppants among other factors [34, 2]. It is practically impossible to model this complicated process without making certain assumptions in an effort to simplify the problem while capturing the major characteristics of hydraulic fracture geometry. Since it is currently not possible to carry out a direct accurate measurement of the fracture geometry during and after the fracturing process, it is customary to use models, with underlying assumptions, to provide some estimation of the fracture dimensions. There are various models used in the industry, however, three classical models are most common because of their relative simplicity, usefulness in bench-marking numerical algorithms as well as for analyzing the

influence of the various problem parameters and the existence of different regimes of fracture propagation. These are the Khristianovich-Geertsma-de-Klerk (KGD) model, Perkins-Kern-Nordgren (PKN) model and the penny-shaped or radial crack model. In all three classical models, rock deformation is described by theory of elasticity, the fluid flow in the fracture is modeled by Poiseuille's law, and the leak-off process follows Carter's leakoff rate [43].

2.2.1 Khristianovich-Geertsma-de-Klerk (KGD) Model

The KGD Model (see Figure 2.1) is a vertical fracture with an infinite height [27, 34]. The crack has an elliptical horizontal cross-section and a rectangular vertical cross-section if the pressure in the crack is uniform. The model assumes that the width of the crack at any distance from the well is independent of the vertical position, i.e. along the fracture face in the vertical direction. This assumption is reasonable for a fracture with a height much greater than its length, thus can be described as a 2D plane strain crack in the horizontal plane. The classical model also incorporates fracture tip effects in which a small region near the crack tip is not penetrated by the fracture fluid as such is modeled as zero fluid pressure. Fluid flow is assumed to be one-dimensional along the fracture length in the classical KGD model.

2.2.2 Perkins-Kern-Nordgren (PKN) Model

The PKN model is a vertical fracture with a constant height independent of fracture length [27, 34].The fracture height is constrained by the higher horizontal stresses in the adjacent layers above and below the reservoir layer. The model assumes elliptical cross sections both in the vertical and horizontal planes when the fluid pressure in the fracture is uniform. In a situation when the fluid pressure is non uniform (i.e. the effect of viscous dissipation is significant), the cross-sections are not elliptical. The crack model is appropriate for a fracture whose height is much more smaller than the length and as such can be modeled as a 2D plane-strain fracture in the vertical plane. The classical PKN assumes fluid flow is one-dimensional along the fracture length.

2.2.3 Penny-Shaped Crack Model

The radial crack or penny-shaped was first presented by Sneddon and Elliot [55]. This crack is assumed to propagate within a plane and it is symmetrical around the injection line source or wellbore if the fluid pressure and injection rate is constant.

With advancements in numerical modeling enhanced by greater computing powers, these classic models originally developed for homogeneous, isotropic and elastic rocks have been improved upon with many of the assumptions relaxed to pave the way for more realistic conditions. Other models such as Pseudo 3D and full-fledged 3D are also popular. As mentioned earlier, the

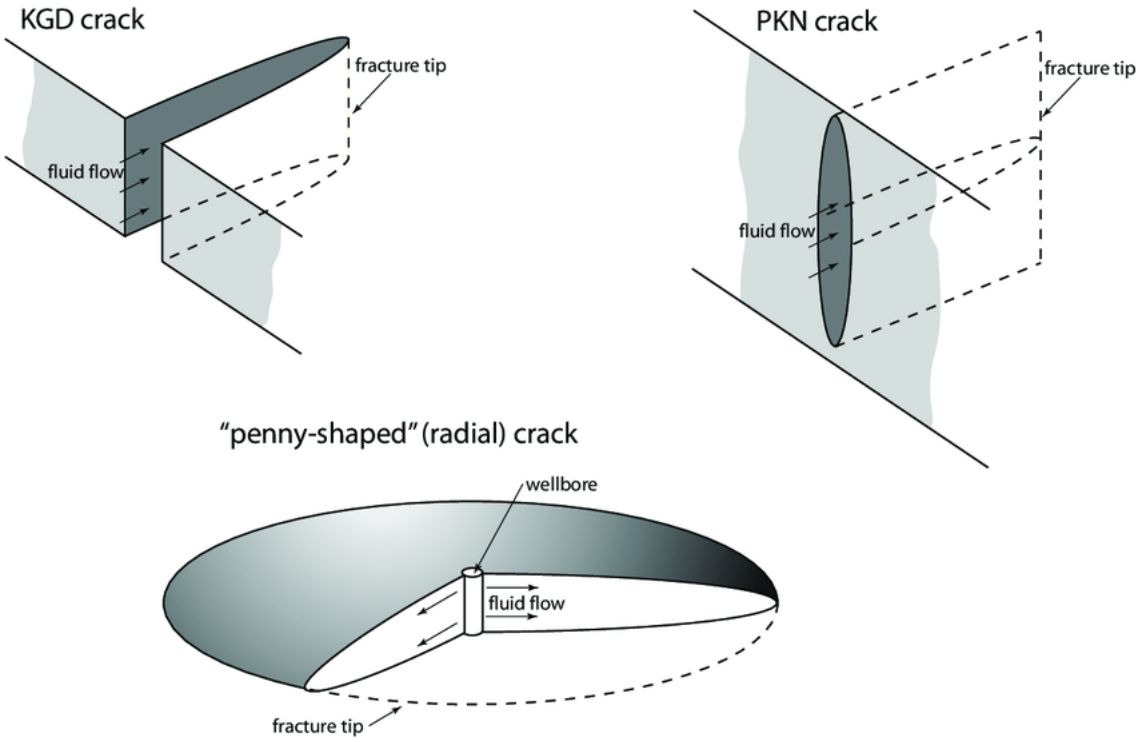

Figure 2.1: Classic fracture models (after Adachi [2])

3 classic models, however, still remains relevant for benchmarking and validation purposes.

2.3 Stress Re-orientation Around Production and Injection Wells

Stress re-orientation describes the conditions in which the direction of the in-situ principal stresses change from their initial or original orientation [24]. It is well established from field observations that the injection/production of fluid in/out of the reservoir changes the pore pressure of the reservoir. The changes in pore pressure subsequently produces stress redistribution in the medium due to poroelastic coupling between the two variables and by extension influences the direction of the local principal stresses. This behaviour is better understood from a poroelastic standpoint. When a load (e.g fluid pressure) is applied to a poroelastic medium, the medium attempts to compensate for the loading by distributing the applied load to its constituents (in-situ pore fluid and solid grain component) [10]. The changes in the pore pressure due to the addition or removal of fluid not only induces a strain on the medium but also changes the stress state because these variables are usually coupled. Since principal stresses dictate the direction a fracture will grow, it is expected that fractures placed in or around such wells will be accordingly influenced. This further implies that in a reservoir with multiple wells, the orientations of the fractures in the different wells will be varied as dictated by the local stress regimes around the

wells.

The impact of these stress perturbations has been a subject of study by many researchers with the aim of understanding how these changes affect well planning, fracture propagation, completion, production and overall reservoir maintenance strategy. One approach often adopted is to study the stress trajectories around the wells in order to infer possible fracture propagation paths. While the stress trajectory can provide an approximation of the fracture path under certain conditions, a full numerical modeling is usually required to determine the actual fracture path. A review of previous work done around stress re-orientation is presented as follows.

Bouteca et al [11] provided a mathematical model to describe fracture reorientation as well as laboratory and field experiments to demonstrate fracture direction control due to induced stress reorientation. They were able to successfully link two wells in a coal seam by hydraulic fracture to enhance coal gasification.

Warpinski and Branagan [62] suggested taking advantage of stress reorientation in the perturbed region to create a desirable fracture orientation. This process was referred to as altered stress fracturing. It is a concept whereby a hydraulic fracture in one well is reoriented by another hydraulic fracture in a nearby location. They conducted a field test to validate the idea and found that it is possible to influence the direction of a fracture by altering the stress state in the medium.

Elbel and Mack [28] addressed the issue of fracture reorientation during refracturing treatment. They suggested that horizontal stress changes due to production creates favorable conditions for refracturing treatment orthogonal to the initial fracture treatment. They observed that during production, the maximum horizontal stress decreased faster than the minimum horizontal stress, thereby causing a stress reversal (switching of directions of the principal horizontal stresses compared to their initial direction) in the neighborhood of the fracture. This makes it possible to initiate and propagate a fracture orthogonal to the initial fracture within the stress reversal envelope.

Bruno and Nakagawa [12] also conducted laboratory experiments in which a propagating fracture which was initially equidistant between an injector and a producer propagated towards the injector due to the higher pore pressure field around the injector. With increased and sustained injection pressure, they observed the fracture was eventually attracted by and ended up in the injector. They attributed this behavior to the local pore pressure gradient at the crack tip. This assertion however was disputed by Detournay and Boone [21] who argued that the pore pressure field near the fracture tip could not have been responsible for the fracture's direction of propagation because the pore pressure field is not singular.

Later, Berchenko and Detournay [7] provided some rigorous mathematical models to describe

and analyze the poroelastic mechanism responsible for the hydraulic fracture deviation. They carried out an analytical study of the stress trajectories around an injector-producer system to predict the fracture's path of propagation and compared the results with numerically computed path. They observed both methods are in excellent agreement provided that a certain dimensionless toughness parameter is small. They summarized their findings by stating that a propagating hydraulic fracture initially equidistant between a producer and an injector will always be deviated by the injector due to the induced stresses in the poroelastic medium. Such a fracture will eventually be attracted by and end up in the injector well if the fracture propagates into an "attraction basin" - a region around the injector well in which all trajectories within it converge to the injection point. This attraction basin was shown to have a stress induced "fracture barrier" characterized by a 90 degree rotation of the principal stress directions along the vertical axis passing through the injector well - thus any stress trajectory that intercepts the "fracture barrier" will be redirected towards the injection point. They concluded that the fracture orientation is controlled primarily by two dimensionless parameters: the ratio of the stress deviator at infinity to the characteristic poroelastic stress associated with the injection and production of fluid and the dimensionless time.

Siebrits et al [53] investigated some factors affecting the azimuth and length of a secondary fracture during a refracture treatment in the neighborhood of a fractured vertical well. They developed 2D and 3D models to determine the necessary conditions to initiate a secondary fracture orthogonal to the primary fracture and its potential growth path. They concluded that three dimensionless groups are the primary influencers of the fracture path in the 2D model − the dimensionless far-field stress deviator, dimensionless time and a dimensionless toughness parameter. For the 3D model, two additional dimensionless parameters; dimensionless fracture height ratio and dimensionless shear modulus ratio were shown to influence the fracture path as well. Their 3D model was used to quantify the stress reversal region (pore pressure induced stress maps) around the initial fracture in a reservoir bounded by confining layers with different mechanical properties. They concluded that the stiffer the confining layers, the smaller is the region with stress reorientation around the fracture. They also suggested some optimum requirements for selecting a well for refracturing purposes.

Several field studies have been carried out in the field to validate the stress field re-orientation concept. Wright and Conant[63] examined tiltmeter readings from five refractured wells where initial tiltmeter data, prior to refracturing were available. They inferred a 30 - 40 degree variation in the refracture dip angle compared to the initial fractures. In another field tiltmeter data examination for a large scale waterflood operation, Wright et.al [1] provided additional evidence of fracture reorientation in fractured infill wells . They compared tiltmeter readings prior to

and after waterflooding and inferred that fracture azimuths could vary as much as 60 degrees from the original fracture orientation and cause horizontal fractures to propagate in areas where vertical fractures were predominant. Fracture dip and strike were also influenced by the local stress changes induced by the pore pressure gradients.

It is worth noting that tiltmeter readings provide average values for fracture orientation. A refracture may indeed be initiated orthogonal to the old fracture due to the strong stress perturbation closer to the initial fracture but as it grows outside of that region it will gradually re-orient itself back to a direction parallel to the old fracture. The tiltmeter would only provide an average orientation values depending on the extent of refracture propagation.

Minner et al [42] yet corroborated the effects of poroelastic stress changes in fracture geometry by examining a data-set of 76 fracture treatments in 12 infill wells. They further confirm that not only were there stress reorientation but also that the fracture orientation depends on the pattern of injectors and producers and their interaction. They found that hydraulic fracture azimuth variability is significantly smaller in infill inline wells placed along the injector rows compared with offset wells placed along the producer rows.

Nicolas and Mukul [45] studied the combined effects of open propped fractures (mechanical effects) and injection/production of fluids in the reservoir (poroelastic effects) on stress perturbation around a fractured vertical well. Their focus was to couple both effects and quantify the stress redistribution around the production wells. They validated their models with field tiltmeter data confirming the presence of a refracture reorientation in the formation. They also provided some guidelines in the selection of an ideal well for refracturing as well as the timing and possible estimates of production increase after refracking.

Sarvaramini and Garagash [48] studied the problem of transient pressurization of a pre-existing, PKN crack in a poroelastic medium due to constant fluid injection. They examined the effect of 2-D leak off (at large times) on poroelastic backstress which was shown to confine the crack. They also examined the effects of poroelastic backstress on the evolution of the fluid pressure in the crack and the initiation of fracture propagation. They compared their solutions to a similar finger-like crack problem in a non-poroelastic medium[47] and concluded that poroelasticity has a minor effect on the fluid pressure evolution in the crack. However, it was shown that poroelasticity does have a significant impact on the evolution of the fracture volume and the onset of the fracture propagation. The induced poroelastic backstress hindered both quantities at large times as the fluid diffusion could no longer be described as 1-D.

Li et al. [65] used a coupled poromechanical model to examine stress redistribution associated with refracturing and the optimal refrac timing . Bearing in mind the time dependency of the stress reorientation, they observed that pressure depletion and the Biot coefficient have positive

correlations with the optimal refracturing time, while the horizontal stress ratio and Poisson's ratio have negative correlations with the time. Permeability and porosity were shown to have no effect on the size of the stress reversal zone but are negatively and positively correlated to the refrac timing, respectively.

Wang et al. [59] investigated parameters affecting the direction of propagation of a refracture including the initiation angle, stress anisotropy, production time and the mechanical effects of propped fractures. They observed that the stress difference and the initiation angle have an inverse relationship with the diverting radius of the refracture (i.e. how far out the refracture travels perpendicular to the old fracture before turning in the direction of the maximum principal stress outside the stress reversal region). The larger the stress difference between the horizontal maximum and minimum stresses, the smaller the diverting radius and vice versa. conversely, the larger the initiation angle (assumed to be the perforation angle), the larger the diverting radius, with an initiation angle of 90 degree being the most favourable. Mechanical effects were shown to have a detrimental influence on the orthogonal propagation path of the refracture.

2.4 Refracturing on the Field

It is well documented from field experiences that when hydraulic fracturing is implemented in wells, there is an initial increase in the production rates of those wells followed by a sharp decline, which often necessitates the implementation of additional stimulations [58, 63, 1, 26]. Refracturing or refracking is one of those re-stimulation techniques that is often employed to mitigate production decline and restore well productivity. Steep production decline associated with the initial fracturing are often a result of inadequate treatment and ineffective or damaged proppant in the fractures[26, 25]. Although refracturing has been in practice for several decades, the use of the technique declined starting from the 1990's till late 2000's due to improvements in hydraulic fracturing design, implementation and maintenance[41]. A renewed interest in the technique was awakened by the oil market collapse in 2014 which forced field operators to explore effective means to enhance production while keeping cost low[37, 64].

Three main factors have been identified as key drivers for refracturing adoption among operators: economic scale, technical feasibility and risks [41]. The economics of refracturing is perhaps the biggest factor, from a global oil price standpoint, associated costs with implementing a refracturing job (usually costs less that 40 % of a new well) as well as the overall rate of return on investment. The technical feasibility involves understanding how to select the best wells for refracturing, fracture reorientation and conductivity, proppant selection and diversion techniques among others. The risk of failed treatments which could include loss of production in the original well or reduced production in neighboring wells as observed in many field trials has

hampered adoption among many operators. Lack of proper understanding of the stress distribution in the reservoir coupled with poor candidate well selection and poor refracturing design have been the leading causes of failures [58].

2.4.1 Design Considerations in Refracturing

The advancement in fracturing technologies in recent times which has made it possible to pump more proppant and fluid as well as design tighter cluster spacing in extended lateral lengths to improve production outcomes have influenced many field operators to conclude that older generation wells may have been understimulated and as such they could be good candidates for refracturing in order to recover stranded reserves. For the refracturing exercise to be successful, there is need for adequate refracturing design.

There are four main steps followed by operators in the design and implementation of a refracturing job. They are (1) candidate well selection, (2) choosing an appropriate treatment system (fluid type and volume, proppant types and sizes and perforation scheme), (3) designing effective isolation and diversion techniques (4) Diagnostics and post refracture evaluation and optimization [32, 41, 51].

2.4.1.1 Candidate Well Selection

Selecting the ideal well for a refracturing operation is perhaps the single most important factor in determining the success of the operation. Not all production wells are ideal for refracturing [58] and as such a careful analysis must be carried out in deciding on which well(s) to choose for a refrac. This typically involve analyzing rock properties (type, stress anisotropy, mechanical and petrophysical properties) and previous stimulation history (fracturing fluid and proppant types, initial fracture geometry, fracture complexity, leak off data, perforation strategy, proppant placement and contribution of perforation clusters) and if there are any naturally fractured zones and water producing zones in the vicinity of the refracture job [51, 41].

Several concepts have been proposed by different investigators to aid the selection process, some of which are reviewed below.

Gas Research Institute (GRI) proposed a three-level analytical approach to help identify the best candidates [44]. Level 1, referred to as rapid screening or statistical production data analysis entails analyzing the early and late time production performance of each well compared to it offset wells. This method could help identify under-performing wells in reservoirs with consistent completion/stimulation methods. The downside of this approach is that it often would miss production wells that are performing well, which could actually benefit more from a restimulation. Level 2 also known as advanced screening uses artificial neural networks and genetic algorithms to identify potential candidates for a refrac. Various data input parameters

such as location, geology, drilling, completion, stimulation etc. are fed to the model and the production response due to each input is measured to gauge which of the these have the greatest impact. Patterns are then identified to deduce best and worst practices after which potential wells, especially those with 'worst' practices (in drilling, completion and stimulation methods) are curated for refracturing considerations. Reasons for poor performances are also deduced during the advanced screening process with some recommendations of how to fix the identified problems. The downside to this approach is that quality data on all of the different input parameters are often scarce or incomplete, thereby detracting from carrying out meaningful analysis. Level 3 involves the use of production type curve matching which has been developed specifically for hydraulically fractured reservoirs to provide estimates on permeability, skin and drainage area. This approach however, have several shortcomings: (1) models are often idealistic, developed for single layer reservoir (realistically most reservoirs are multi-layer and production often cut across several layers), (2) production data used to develop such type curves often include 'noise' and such data also depend on the unique properties of the reservoirs from which they were obtained. Extrapolating from such type curves to match performance in other wells is often difficult and results may not be unique. While the 3-level analysis showed that poor performers are not necessarily the best wells to select for refracturing, the approach's downside is that each type of analysis selects different "candidate wells" as such rendering the approach inconclusive in its ability to confidently select top candidate wells for refracturing.

Barba and Shook [6] suggested the use of "completion efficiency" concept to screen candidate wells for refracturing. The completion efficiency metric is obtained by dividing the actual production rate by the predicted rate for a minimum acceptable propped fracture length and conductivity. It is a performance evaluation concept that could help identify underlying problems such as low formation capacity (kh), low production pressure and poor initial fracture treatment that may be associated with a subprime performance of a well.

Sinha and Ramakrishnan [54]suggested the use of "completion index" and "production index" to screen potential refrac candidates. They define the completion index as the ratio of the total volume of pumped fluid to the lateral length divided by the number of stages. A cross plot of the the completion index and production index is then used to identify those wells with reasonably high production index but low completion index. One advantage of this approach is that it offers quick screening of potential wells for refrac. A downside to this method however, is that, further and in-depth analysis is often required to further narrow down the list obtained via the method. The impact of stress redistribution, for instance, is not considered in the analysis.

Rousell and Sharma [46] proposed a framework for selecting candidate wells for refracturing using using five dimensionless variables based on historical reservoir properties and production

data. The framework incorporates the effects of stress reorientation, initial completion performance, reservoir quality and neighboring wells production history. They suggested the following dimensionless groupings: Stress reorientation numbers (poroelastic & mechanical), well completion number, reservoir depletion number and production decline number. Apart from stress reorientation numbers, the other 3 parameters are well specific and is typically calculated for each well.

While different candidate well selection methods seem to differ in some ways, we see a common list of factors to consider while making the selection. These include reservoir properties(petrophysical, fluid, mechanical), the initial completion and production data. Since there is no widely accepted approach of selecting candidate wells, multiple method could be used concurrently with the aim of selecting those wells that show up across all models. The underlying assumptions in these selection models should be understood before choosing one model over another.

The use of Artificial Intelligence (AI) to aid candidate well selection has been proposed by a number of researchers [49, 66]. With the tremendous amount of production and completion datasets, there seems to be an opportunity for machine learning algorithms to ingest these data to aid predictive analytics and modeling of refracturing operations. Aryanto et al [4] and Gupta et al [33] presented cases studies where AI algorithms were used to rank candidate wells considered for fracturing operations. These AI-powered models integrates reservoir and production data to learn patterns and transfer such knowledge into workflows that improves production efficiency. Due to the fact that AI adoption in the oil and gas industry is still in its infancy stages, extensive development of the tool and its application to different aspect of oil and gas operations, particularly hydraulic fracturing is yet to be seen. Convincing case studies need to be published before operators can begin to consider broader adoption of the tool to their existing operational workflows.

2.4.1.2 Refracture Treatment System

This step involves deciding on the best fracturing fluid and proppant types for the job in order to attain the overall design objective. A thorough understanding of the reservoir properties (mechanical and petrophysical) and the initial well completion strategy is vital in the success of this phase of the refracturing process.

Fracturing Fluid

Fracturing fluid aid in initiating and extending fractures as well as placing proppants inside the fractures. The reservoir geomechanical properties, rock type, stress state, reservoir fluid and intended fracture geometry are all important factors that must be carefully considered when

designing an appropriate fracturing fluid. [36, 32]. For instance, reservoirs with high stress anisotropy and a greater degree of ductility, will typically require a high viscosity fluid if the goal is to produce thick planar fractures and transport proppants farther into the fractures. Similarly, for more brittle rocks with low-stress anisotropy, low-viscosity fluid such as slick water is often used for refracturing operations in many unconventional plays in other to create complex fractures and transport proppants effectively into the fracture network [41]

Proppant Type

The proppants help keep the fracture open and conductive once the fracturing fluid is dissipated. The proppant type, strength and size as well as fracture geometry, formation and fracturing fluid properties are important factors to consider when choosing the appropriate proppants for any fracturing job. [50]. Ductile formation with high stress anisotropy typically requires a larger proppant size e.g. 20/40 mesh with more viscous frac fluid to create and extend wider fractures. For refracturing jobs especially in more the brittle formation and fairly isotropic stress conditions where more complex fracture networks are expected, smaller proppant sizes e.g. 40/70 or 70/140 mesh are often used [41]. High concentrations of smaller proppant sizes are favored in wells initially fractured with larger proppants [61, 20].

2.4.1.3 Isolation and Diversion Technique

The objective of the refracturing exercise often dictates what type of isolation technique to deploy. In cases where the goal is simply to reopen, extend or increase proppant concentration in the existing fractures, the standard "plug and perf"" method is the preferred choice because of the flexibility in designing and implementation. However, for a refrac whose goal is to access new sections of the wellbore not previously fractured, there is a need to isolate the existing perforations for the planned restimulation to be effective. There are four main methods used to isolate previous perforations.

The first approach involves pumping cement into the existing perforations to seal them off. Once the cement is set, the reminder cement in the wellbore is drilled out so that the well can be re-perforated to allow reservoir fluid flow into the well. While this approach is fast and cheap, it has a major drawback [67]. Because cement contains solid particles, the tendency for bridging over the proppant pack in the main fractures is high and thus often lead to ineffective seal of the perforations as the cement may not be able to block off the microcracks leading to the main cracks. This often results in leaks and sometimes the ultimate failure of the procedure.

The second isolation technique is the use of mechanical barriers to isolate existing perforations [67, 51]. This involves running an expandable liner with a smaller outer diameter than the inner diameter of the production casing across the perforated internals to provide a seal. Once the liner

reaches the target perforated interval, it is expanded against the wall of the casing to provide a patch that seals off the perforations. This is repeated until the entire perforated sections are sealed off. New perforations are added and treated with proppant slurries to create new fractures after which the liners are mechanically removed from the well to provide access to old fractures for fluid flow into the wellbore. While this method is quite effective, it has some drawbacks as well. Costs could be prohibitive if there are numerous perforated stages and clusters on the production casing. A second potential drawback is the possibility of damaging the cement integrity of the casing. During the expansion of the liner against the walls of the casing, the casing wall itself expands against the cement which upon the relieve of the pressure may create flow pathways behind the casing.

The third isolation method is the use of straddle packer on a coiled tubing [67, 51]. The straddle packer can isolate specific sections of the wellbore so that fluid and proppants can be directed appropriately to target zones. The entire refrac job is pumped down through the coiled tubing, which characteristically, has very small internal diameter and thus the pumping rate will be much lower due to pipe friction. This in turn results in smaller and shorter fractures being created as high pump rates and large proppant concentrations are often required for larger fractures. Longer treatment duration as a result of smaller pump rates may lead to increased operational costs.

The fourth method is the use of degradable polymer diverters or particulates [50, 29]. These are specially formulated chemicals that have the ability to solidify under certain conditions and stay solid for a period of time before dissolving back to liquid forms. One of the most popular chemical used as a diverter is the polylactic acid or polylactide due to its self-degradable ability as well as ease with which its composition could be modified to suit various reservoir temperature and pressure conditions. Chemical diverters are pumped down into existing fractures to provide a temporary seal through the mechanisms of 'jamming' - larger molecule particulates bridge the flow paths between proppants thereby forming a base structure for the finer molecule particulates to settle and provide a complete seal for any remaining flow paths ('plugging'). Once the polymers are set, new stages can be fractured and treated with proppants. The main advantages of this method are that they are cost-effective, environmentally friendly and capable of withstanding high treatment pressure and temperatures[51, 50] and will self-degrade over a controlled period of time to re-establish the flow paths to the old fractures without any damage to the reservoir or the casing. There are however some major drawbacks for chemical diverters. The success of the technique is significantly dependent on thorough understanding of the formation fluid and mineral properties as these could interact with the chemical compositions of the diverters thereby altering their properties and ultimately affecting their performance as a

sealant. Unlike mechanical diverters, chemical diverters cannot be randomly applied to different formations without first understanding the formation chemistry; this additional knowledge gap, may hinder a widespread adoption.

2.4.1.4 Diagnostics and post refracture evaluation and optimization

One critical component of the refracturing enterprise is the ability to monitor the progress and evaluate the success of the operation real-time. Diagnostics methods are broadly grouped into direct far field, direct near wellbore and indirect techniques [17, 41].

Direct far-field monitoring involves the use of tiltmeter, accelorometer and/or geophones to measure tilt (deformation) and microseisms in the rock mass during a refracturing job. Such diagnostics are conducted from offset wellbores or from the surface while the refracturing operation is underway to provide a bird's eye view of the fracture growth and direction, that is the data obtained from these measurements are anaylsed and inferences are drawn about the fracture characteristics such as length, geometry, azimuth and dip. Moreover, the distribution of microseismic events locations can help identify which part of the well is being restimulated. Microseismic mapping can also help to track the effectiveness of diverter for zonal isolation [51]. A major drawback of direct far-field monitoring is that they do not provide any insight into the effective propped fracture length and it conductivity [17]. Another draw back is that their mapping resolution decreases the farther they are away from the refracturing treatment source.

In direct near-wellbore monitoring, specific physical properties such as temperature or radiation are logged directly from the the treatment wellbore after the refracturing treatment. One significant merit of this technique is its ability to accurately identify fluid/proppant entry intervals as well as production from each zone in a well with multiple zone completions. For instance, because frac fluids have lower temperatures than the formation, it is possible to track which perforations zones are receiving the most fluid by monitoring the change in temperature. The zone with the biggest temperature drop is the zone taking the most frac fluid. The downside of this technique, however, is that it has very low resolution depth and cannot 'see' beyond about 2 feet from the wellbore and such may not provide meaningful fracture characteristics. It may, however, provide a lower-bound estimate of fracture height if the well and the fracture are misaligned [17].

In indirect fracture monitoring technique, pressure response and flow rate measurements are inverted to estimate fracture dimensions and conductivity. The dataset needed for such analysis are readily available from the fracturing operations and production data. Observed data are compared with reservoir/ fracture models to estimate the fracture characteristics. Example of analyses carried out in this category are fracture net pressure analysis, pressure transient testing and production data analysis [17]. The major drawback of this method is that analytical

or numerical solutions obtained from modeling are not usually unique and therefore must be calibrated with direct observations.The indirect approach, however, can be a very useful tool once calibrated to detect refracture-treatment problems as well as re-fracture optimization workflows.

2.5 Theory of Linear Poroelasticity

The theory of poroelasticity captures the various interactions between the solid and fluid component of the poroelastic media. It is a framework used to understand the deformation/diffusion processes fluid-filled porous rocks undergo when subjected to different loading conditions. In-situ hydrocarbon rocks are always under stress and are usually saturated with fluids - oil, gas or water, as such, their behaviour is more realistically studied under the poroelastic framework.

Poroelasticity has been widely studied in hydrogeology and geomechanics. It is well known that the injection or extraction of fluids from a fluid-saturated rock formations induces stress changes, pore pressure changes as well as deformations in the porous media [23, 60]. The changes in these variables (stress, strain, pore pressure and fluid content) are often coupled such that a change in one variable produces a change in another and ultimately influence the mechanical and volumetric response of the porous medium. These coupling - *solid-to-fluid* (a change in applied stress produces a change in pore fluid pressure and fluid mass) and *fluid-to-solid* (a change in fluid pressure induces stress and rock deformation) - are central in the study of poroelasticity.

There are two limiting states of describing a poroelastic medium : *undrained* and *drained* states. A fluid infiltrated porous medium is said to be in an *undrained* state when the trapped fluid in its pore spaces are prevented from escaping after a loading has been applied to it. This behaviour is also observed when there is a sudden application of a loading on a fluid-filled porous material. The trapped fluid does not have sufficient time to escape and as such this leads to an excess pore pressure build-up (Mandel-Cryer effect) and thus the material appears to be 'stiffer'[60]. On the other hand a material is said to be in a *drained* state if all the excess fluid pressure are allowed to dissipate. Such drained materials appears to be 'softer' compared to its undrained state. It is obvious from the foregoing that these mechanism will introduce some time-dependency on the mechanical and volumetric response of a fluid-saturated poroelastic material.

A poroelastic medium can be characterized with numerous material property constants. However, only four of such constants can be independently selected while the other variables can be derived from different combinations of the independent constants. Different authors [23, 19, 18, 30, 10] seems to adopt unique sets of the independent material constants for their constitutive equation formulations depending on whether the fluid or the solid component response is being modeled. For instance Detournay and Cheng [23] adopted the drained bulk

modulus, K, undrained bulk modulus, K_u, and the Biot's coefficient, α, as a fundamental set for modeling the volumetric response of a poroelastic media. In modeling the mechanical response, they adopted drained Poisson ratio, v, undrained Poisson ratio,v_u, shear modulus, G, and Biot's coefficient,α. In this work, we adopt the Detournay and Cheng fundamental sets. There are other material constants that are very important in formulating poroelastic equations, even though, they are dependent on the fundamental set. Three of such that will be used in this thesis are poroelastic stress constant, η, uniaxial specific storage coefficient, S and the Skempton's pore pressure coefficient, B.

A brief description of the material constants used in this work are presented below with their formulas given in appendix A [60].

- Biot's coefficient, α: a ratio of pore volume change (increment in fluid content) to bulk volume change at constant pore fluid pressure. It describes how effective the pore fluid could 'cushion' the effect of the total applied stress on a fluid-saturated media. It is often used in the calculation of effective stress. It is dimensionless and its value ranges between 0 and 1[23].

- Poroelastic stress constant, η: this dimensionless parameter controls the value of stress changes induced by pore pressure changes as a result of fluid injection, production or fracture fluid loss [23, 27]. It is a function of the Biot's coefficient and the Poisson ratio of the porous media .

- Uniaxial specific storage coefficient, S: a measure of the amount of fluid that must be added or removed from a rock sample under uniaxial strain and constant vertical stress to produce a given fluid pressure change. It controls the amount of fluid that can be stored in or released from storage as the uniaxial constraint (zero lateral strain) limits the extent of pore volume change. It has the unit of [pressure]$^{-1}$. In the limiting case where $v \simeq v_u$, the inverse of the storage coefficient is called the Biot Modulus, M.

- Undrained Poisson ratio, υ_u: whereas the drained Poisson ratio,υ(same as in elasticity) describes the ratio of lateral strain to longitudinal strain under axial loading, the undrained Poisson ratio,υ_u, describes such deformation for a fluid-saturated media by taking into cognizance the presence of the fluid which is prevented from escaping during the loading process. It is a parameter that captures the interaction between the solid skeleton and the fluid in the pore spaces of a medium.

- Drained bulk modulus, K, as in elasticity, is a measure of the poroelastic medium's ability to resist compression or change in volume when under external loading after the pore fluid

had escaped as a result of the loading . It is the ratio of a small increase in pressure to the resultant relative decrease in a drained elemental representative volume of the poroelastic medium.

- Undrained bulk modulus, K_u, similar to K, except that the fluid in the pore spaces are prevented from escaping while the representative elemental volume is under compression. It is a measure of the medium's compressibility while fluid is trapped in the medium.

- Shear modulus, G, as in elasticity, is the measure of the rigidity or shear deformation of the poroelastic medium while under shear stress. It is generally expressed as the ratio of shear stress to shear strain acting on the representative elemental volume of the medium.

Chapter 3

Poroelasticity and Boundary Integral Equations

There are four key equations governing the behaviour of a fluid-saturated poroelastic media. They are the constitutive relations between the stress, strain and pore pressure, force equilibrium equations, fluid flow equation and continuity equation [60, 23]. These four equations when combined forms the field equations that needs be solved to quantify the various field quantities that describe the poroelastic model.

3.1 Governing Equations of Linear Isotropic Poroelasticity

In this section a brief description of the four equations that forms the the governing equations for poroelasticity is provided.

3.1.1 Constitutive Equations

Constitutive equations in poroelasticity relates stress, strain and pore fluid pressure to describe the response of the poroelastic material to applied loads. There are two types of responses: the response of the solid component to applied loads and the response of the fluid component to the applied loads. Thus, there are two constitutive equations to describe a poroelastic material unlike in the case of elasticity where only one of such equation is required. Furthermore, the first equation relates solid strain to total stress and pore pressure and the second relates the variation of fluid content to pore pressure and solid volumetric strain [23, 31]. The following formulations have ignored body forces and fluid sources within the representative element of the poroelastic media.

The general form of these equations are given by Detournay and Cheng [23] either as a strain-stress relation (3.1) or a stress-strain relation (3.2)

$$2G\varepsilon_{ij} = \sigma_{ij} - \frac{v}{1+v}\sigma_{kk}\delta_{ij} + \frac{\alpha(1-2v)}{1+v}p\delta_{ij} \tag{3.1}$$

$$\sigma_{ij} + \alpha p\delta_{ij} = 2G\varepsilon_{ij} + \frac{2Gv}{1-2v}\varepsilon\delta_{ij} \tag{3.2}$$

The above constitutive expressions can be reduced to the plane strain equivalent by noting that the strain $\varepsilon_{13} = \varepsilon_{23} = \varepsilon_{33} = 0$ and the subscripts i, j, k take on the values 1 and 2, while the out of plane normal stress, σ_{33} becomes

$$\sigma_{33} = v\sigma_{kk} - \alpha(1-2v)p, \qquad k = 1, 2 \tag{3.3}$$

Thus, for plane strain, equations (3.1) and (3.2) becomes

$$2G\varepsilon_{ij} = \sigma_{ij} - v\sigma_{kk}\delta_{ij} + \alpha(1-2v)p\delta_{ij} \tag{3.4}$$

$$\sigma_{ij} + \alpha p\delta_{ij} = 2G\varepsilon_{ij} + \frac{2Gv}{1-2v}\varepsilon\delta_{ij} \tag{3.5}$$

Note equation (3.5) is the same as (3.2) with the only difference in the range of i, j which are now 1, 2

The response of the pore fluid to the applied loads can be expressed also in two forms, depending on whether the mean stress or the volumetric strain is used as the coupling term [23]. The preferred expression used in this work is given as

$$p = M(\zeta - \alpha\varepsilon) \tag{3.6}$$

where ζ is the increment or variation in fluid content per unit reference volume.

3.1.2 Equilibrium Equations

A representative elemental volume (REV) of a poroelastic medium subjected to stresses is usually, in static translational and rotational equilibrium at any instant in time. Such medium is in static equilibrium if the body is not accelerating and the net forces acting on it is zero and it is in rotational equilibrium if the stress tensor is symmetric. These conditions needs must be true for the medium to be deemed in equilibrium. The equilibrium equation, assuming zero body forces is given by

$$\sigma_{ij,j} = 0 \tag{3.7}$$

The subscript i, j ranges from 1 to 3 for a 3D model and 1 to 2 for a 2D plane strain formulation.

3.1.3 Fluid Flow Equation

The fluid flow in the poroelastic medium is generally governed by Darcy's law which states that the fluid flux across a cross-sectional area is directly prosegmental to the pressure gradient. Fluid flow in the medium is assumed linear. Again, assuming zero fluid body forces, this can be written mathematically as [23]

$$q_i = -\kappa p_{,i} \tag{3.8}$$

where $\kappa = k/\mu$, is the permeability coefficient, k, is the intrinsic permeability of the medium and μ, is the viscosity of the fluid in the medium.

3.1.4 Continuity Equation

The continuity equation is a mass conservation equation of the fluid flowing into and out of a representative elemental volume. This is given as

$$\frac{\partial \zeta}{\partial t} + q_{i,i} = 0 \tag{3.9}$$

where ζ is the variation of the fluid content which describes the increment of fluid volume per unit volume of the porous medium [9] and q is the specific discharge. The above equation assumes there is no source density within the elemental volume.

A combination of the four governing equations produce two field equations expressed in terms of displacement vector (i.e a Navier- type equation) and the pore pressure (a diffusion equation).

Navier Equations The solid strain can be expressed in terms of displacement components as

$$\varepsilon_{ij} = \frac{1}{2}(u_{i,j} + u_{j,i}) \tag{3.10}$$

By combining the equilibrium equation (3.7) and the constitutive equations (3.1) with strain expressed using (3.10), we obtain the Navier type equation for the displacement as

$$G\nabla^2 u_i + \frac{G}{1-2v} u_{k,ki} = \alpha p_{,i} \tag{3.11}$$

Diffusion Equations Two diffusion equations can be derived; one in terms of pore pressure, p, and the other in terms of variation of fluid content, ζ. In this work, we focus on the diffusion equation derived in terms of pore pressure. The combination of the constitutive equation (3.5), flow equation (3.8), and continuity equation (3.9), produces the coupled diffusion equation given

as [23, 16]

$$\frac{\partial p}{\partial t} - \kappa M \nabla^2 p = -\alpha M \frac{\partial \varepsilon}{\partial t} \tag{3.12}$$

Equation (3.12) indicates that the diffusion of pore pressure is coupled with the rate of change of the volumetric strain. Under certain conditions, the pore pressure field can be uncoupled from the displacement field [16, 60] . This condition exists if one of the boundaries of the problem's domain is infinite. By noting that the right side of (3.12) is purely time dependent, at infinity, the change in volumetric strain is zero as such the equation can be reduced to:

$$c\nabla^2 p - \frac{\partial p}{\partial t} = 0 \tag{3.13}$$

Where, $\kappa M = k/\mu S = c$. The constant, c is the diffusivity coefficient and S is the uniaxial specific storage coefficient which is approximately $1/M$ when $v_u \simeq v$.

Equations (3.11) and (3.12) for the basic set of equation which when solved together using the appropriate boundary and initial conditions, would produce solutions for the displacement and pore pressure field.

3.2 Solution to the Poroelastic Field Equations

To aid in the solutions of the these equations, fundamental solutions (also known as free-space Green's function) are of the essence [15, 31]. These are solutions derived using various singular impulses at a point in an unbounded domain with no particular boundary condition to satisfy. These fundamental solutions are well behaved everywhere in the problem domain except at the point of application of the impulse where there is a mathematical singularity. Common impulses used are the point force, dipoles, point fluid source and point displacement discontinuity to name a few.

3.2.1 Boundary Integral Equations (BIE)

To attempt a solution to the field equations, the partial differential equations (PDE) in (3.11)and (3.13) are recast in boundary integral forms using the rigorous reciprocal theorem or heuristic superposition theory [15]. The boundary integral equations are set up by convoluting the fundamental solutions and the source densities distributed along the boundaries of the problem domain in time and space [23, 57]. Once the densities of these impulses are known, it is possible to determine other field quantities such as stress, fluid flux, pore pressure and displacement using the superposition principle. The fundamental solutions used in this work have already been derived by Cheng and Detournay [15, 16] and are provided in Appendix B.

To formulate the BIE for a fractured injector or producer well problem, consider a fracture

whose boundary is denoted by Γ in a poroelastic medium . We can write a boundary integral representation of the solution for the stress and pore pressure fields around the fracture by using the fundamental solutions and the source densities distributed along the locus of the fracture as follows:

$$\sigma_{ij}(\mathbf{x},t) = \int_0^t \int_\Gamma \sigma_{ijk}^{ip}(\mathbf{x},\chi;t-\tau)F_k(\chi,\tau)d\Gamma d\tau + \int_0^t \int_\Gamma \sigma_{ij}^{is}(\mathbf{x},\chi;t-\tau)\psi^*(\chi,\tau)d\Gamma d\tau \quad (3.14)$$

$$p(\mathbf{x},t) = \int_0^t \int_\Gamma p_k^{ip}(\mathbf{x},\chi;t-\tau)F_k(\chi,\tau)d\Gamma d\tau + \int_0^t \int_\Gamma p^{is}(\mathbf{x},\chi;t-\tau)\psi^*(\chi,\tau)d\Gamma d\tau \quad (3.15)$$

where $\mathbf{x}$ and $\chi$are two-dimensional coordinate tensors, $\sigma_{ij}(\mathbf{x},t)$ is the stress component at coordinates $\mathbf{x}$ and time t. $F_k(\chi,\tau)$ and $\psi^*(\chi,\tau)$ are instantaneous point force and fluid source densities respectively located at $\chi$and induced at time τ. $\sigma_{ijk}^{ip}(\mathbf{x},\chi;t-\tau)$ and $\sigma_{ij}^{is}(\mathbf{x},\chi;t-\tau)$ are the fundamental solutions for the stress components induced by the instantaneous point force and fluid source respectively, while $p_k^{ip}(\mathbf{x},\chi;t-\tau)$ and $p^{is}(\mathbf{x},\chi;t-\tau)$ are fundamental solutions for the pore pressure field as a result of the instantaneous point force and fluid sources respectively. The superscript "ip" and "is" represents instantaneous point force and fluid source respectively while the subscripts i,j,k represents directions which ranges from 1 to 2 since the problems considered in this work are in plane strain.

3.2.2 Boundary Element Method

Several solution techniques abound in the literature for solving the resulting boundary integral equations including Finite Element Method (FEM), Extended Finite Method (XFEM) and Boundary Element Method (BEM) to name a few [5, 57, 3, 59]. In this work, boundary element method has been adopted as the preferred method of solution for a couple of reasons. Unlike, FEM which requires full domain descritization, only the problem boundaries need to be descritized in BEM [5, 40]. This implies that the data points and the number of simultaneous equations that needs to be solved are significantly less, resulting in lesser computation time compared to FEM. Since only boundaries are descritized, it is very suitable to solve problems involving infinite domains. While the traditional BEM does have some few drawbacks, one of which is that it has some difficulty in treating nonlinear problems, luckily, the set of problems considered in this work are linear and homogeneous. There are however, extensions of the the traditional BEM that can now handle these difficulties with ease, but those will not be considered in this work. Also the fully populated matrices may require more computing power, but

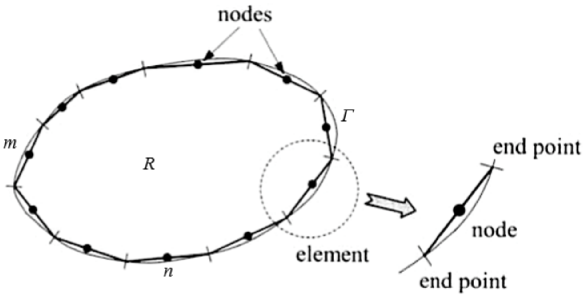

Figure 3.1: Constant boundary element adapted from Katsikadelis [40]

thankfully most modern computers have sufficient storage and memory to carryout the needed computations.

A brief introduction of the Boundary Element Method is provided next. A detailed review of the Boundary element method can be found in literature [40, 5].

Consider a boundary value problem of region R bounded by the boundary Γ with some specified boundary conditions. The solution to the problem is constructed such that the boundary integral equations are approximated by first dividing the boundary Γ, into N number of boundary elements or segments [40]. Three basic element types are commonly used - constant, linear and quadratic elements. Each element is made up of the *end points* and the *nodal points*. The end points mark the dimension of the element and the nodal points are where the boundary quantities are assigned. For the constant element (which is used in this work), the boundary segment is a straight line which connects the end points while the nodal point is located in the middle of the element as shown in Figure 3.1. The linear element also have two end nodes which also doubles as the nodal points where boundary quantities are assigned. The quadratic element has three nodes that serves both as end points and nodal points. The unknown source densities or impulses are then distributed on each element so that the summed effect of all the sources satisfy the prescribed boundary conditions [40]. For the constant element descritization, the source densities are assumed to be constant over each element. The effects of all the N sources are collocated at the midpoint of each element as the problem boundary is traversed from one nodal point to another in an anticlockwise fashion resulting in a system of N linear algebraic equations with the unknown densities as the variables to be solved for. Upon solution, any relevant quantities such as stress and displacement captured in the field equations can then be determined at any point within R or its boundary Γ.

3.2.2.1 Numerical Implementation of BEM

Here we focus on the implementation of the BEM for solving the integral equations derived from the field equations. Since the densities are distributed in space and time, there is a need for both spatial and temporal descritization. The spatial descritization is accomplished by segmenting

the problem boundary into a number of elements and replacing the integrals over the boundary by a sum of integrals. However, the temporal descritization can be avoided by recasting the integral equations in the Laplace transform space so that we only need to carry out a spatial descritization, effectively reducing the problem dimension by one. Once the densities are determined in the Laplace space, they need to be inverted back into the time space for meaningful interpretation.

Taking the Laplace transform of equations (3.14) and (3.15), we can rewrite the equations as

$$\sigma_{ij}(\mathbf{x},s) = \int_{\Gamma} \tilde{\sigma}^{ip}_{ijk}(\mathbf{x},\chi;s)\tilde{F}_k(\chi,s)d\Gamma + \int_{\Gamma} \tilde{\sigma}^{is}_{ij}(\mathbf{x},\chi;s)\tilde{\psi^*}(\chi,s)d\Gamma \tag{3.16}$$

$$p(\mathbf{x},s) = \int_{\Gamma} \tilde{p}^{ip}_{k}(\mathbf{x},\chi;s)\tilde{F}_k(\chi,s)d\Gamma + \int_{\Gamma} \tilde{p}^{is}(\mathbf{x},\chi;s)\tilde{\psi^*}(\chi,s)d\Gamma \tag{3.17}$$

where the tilde overbar denotes the Laplace transform. The fundamental solutions in the Laplace space are provided in Appendix B.

We make the following approximation in the numerical implementation of the BEM: (1) constant straight line boundary elements of equal dimensions are used to segment the problem boundary (2) the fundamental solutions due to the point force and fluid source are applied at the mid nodal point of each element. (3) the source densities are constant over each element and are collocated at the mid nodal point.

With N number of boundary elements and noting that the source densities are constant on each element, the induced stress and pore pressure can be approximated using the following summation;

$$\sigma_{ij}(\mathbf{x}^m,s) = \sum_{n=1}^{N}\left(\int_{\Gamma_n} \tilde{\sigma}^{ip}_{ijk}(\mathbf{x}^m,\chi;s)d\Gamma\right)\tilde{F}_k(\chi^n,s) + \sum_{n=1}^{N}\left(\int_{\Gamma_n} \tilde{\sigma}^{is}_{ij}(\mathbf{x}^m,\chi;s)d\Gamma\right)\tilde{\psi^*}(\chi^n,s) \tag{3.18}$$

$$p(\mathbf{x}^m,s) = \sum_{n=1}^{N}\left(\int_{\Gamma_n} \tilde{p}^{ip}_{k}(\mathbf{x}^m,\chi;s)d\Gamma\right)\tilde{F}_k(\chi^n,s) + \sum_{n=1}^{N}\left(\int_{\Gamma_n} \tilde{p}^{is}(\mathbf{x}^m,\chi;s)d\Gamma\right)\tilde{\psi^*}(\chi^n,s) \tag{3.19}$$

m and n are nodal points of element m and n on the boundary and they range from 1 to N. By introducing the following notation

$$\overset{mn}{A} = \int_{\Gamma_n} \tilde{\sigma}^{ip}_{ijk}(\mathbf{x}^m,\chi;s)d\Gamma \tag{3.20}$$

$$\overset{mn}{B} = \int_{\Gamma_n} \tilde{\sigma}_{ij}^{is}(\mathbf{x}^m, \chi; s) d\Gamma \tag{3.21}$$

$$\overset{mn}{C} = \int_{\Gamma_n} \tilde{p}_k^{ip}(\mathbf{x}^m, \chi; s) d\Gamma \tag{3.22}$$

$$\overset{mn}{D} = \int_{\Gamma_n} \tilde{p}^{is}(\mathbf{x}^m, \chi; s) d\Gamma \tag{3.23}$$

Equations (3.18) and (3.19) can be written as

$$\overset{m}{\sigma}_{ij} = \sum_{n=1}^{N} \overset{mn}{A} \overset{m}{\tilde{F}_k} + \sum_{n=1}^{N} \overset{mn}{A} \overset{m}{\tilde{\psi}^*} \tag{3.24}$$

$$\overset{m}{p} = \sum_{n=1}^{N} \overset{mn}{A} \overset{m}{\tilde{F}_k} + \sum_{n=1}^{N} \overset{mn}{A} \overset{m}{\tilde{\psi}^*} \tag{3.25}$$

A few remarks about equations (3.24) and (3.25).

- The coordinate of the influencing point, χ, changes with each boundary element as the boundary is traversed.
- Boundary conditions needs must be specified to solve for the unknowns $\overset{m}{\tilde{F}_k}$and $\overset{m}{\tilde{\psi}}$. Once solved, a similar equation as in (3.24) and (3.25) can be written to solve for the problem quantities such as displacement, stress, flux etc. at any location with the domain or on the boundary.

Similar formulation can be done for the displacement discontinuity method. The major difference in implementation is the change in the integration kernel from point force fundamental solution to point displacement discontinuity fundamental solution.

Since the goal of this work is to model perturbed stress field around fractured wells due to fluid injection and pumping, the influence of the fluid source will be predominant as such the first part of equations (3.24) and (3.25) may be dropped such that the modified numerical solution to the problem becomes

$$\overset{m}{\sigma}_{ij} = \sum_{n=1}^{N} B_{mn} \overset{m}{\tilde{\psi}^*} \tag{3.26}$$

$$\overset{m}{p} = \sum_{n=1}^{N} D_{mn} \overset{m}{\tilde{\psi}^*} \tag{3.27}$$

Next we consider the inversion of the solution back to time domain.

3.2.2.2 Numerical Inversion of Laplace Transform

There are several inversion techniques to invert functions from Laplace space back to time space. The choice of which inversion algorithm to use is often influenced by the behaviour of

the function to be inverted. For instance Gaver-Stehfest algorithm works excellently well for non-periodic or non-oscillatory functions [56, 39]. The set of problems considered in this work are non-oscillatory as such the choice of the algorithm for the Laplace space inversion. A brief summary of the algorithm is provided as follow.

Given a function $\tilde{f}(s)$ in Laplace domain, we can obtain its equivalent, $f(t)$ in time domain by using the following expression [56, 39]:

$$f(t) \approx \frac{ln2}{t} \sum_{n=1}^{N} V_n \tilde{f}(n\frac{ln2}{t}) \tag{3.28}$$

where the coefficient V_n is given by

$$V_n = (-1)^{n+N/2} \sum_{k=(n+1)/2}^{min(n,N/2)} \frac{k^{N/2}(2k)!}{(N/2-k)!k!(k-1)!(n-k)!(2k-n)!} \tag{3.29}$$

A six-point Stehfest weights, V_n are used in this work. Where $V_{1-6} = 1, -49, 366, -858, 810, -270$.

The solution techniques discussed in this chapter will be applied to problems in Chapter 5 when a fractured producer well is considered. There, the dimensionless versions of the boundary integral equations for stresses and pore pressure are provided and solved using a computer code developed in Mathematica.

Chapter 4

Stress Trajectories and Fracture Deviation Around Unfractured Producer-Injector Well System

4.1 Introduction

In this chapter, the problem of fracture deviation will be examined using the concept of stress trajectories. Specifically, the influence of induced stresses due to the activity of fluid injection and pumping on the stress trajectories around an injector- producer well system will be examined. The problem considered in this chapter was motivated by a previous work done by Berchenko and Detournay in which they studied the deviation of a hydraulic fracture towards an injector well, but initially propagating on a straight course, mid-way between the injector and a producer well. They argued that the change in direction of the fracture towards the injector well was informed by the fact that the injector well, having a higher pressure field around it, creates an *attraction zone*. Thus, any fracture propagating into this zone will be deviated by the stress field around the injector and the fracture could ultimately end up in the injector well. They also concluded that the fracture path can be approximated by the stress trajectory as long as certain dimensionless toughness parameter is small. If the toughness parameter is large, they concluded that a recourse to full numerical fracture propagation modeling should be pursued to predict the fracture path as the stress trajectory would no longer be accurate to predict the fracture path.

In this chapter the Berchenko-Detournay problem was revisited using the stress trajectory to predict fracture propagation direction. While the authors carried out a full numerical modeling of the fracture path in order to account for the effect of large fracture toughness, such

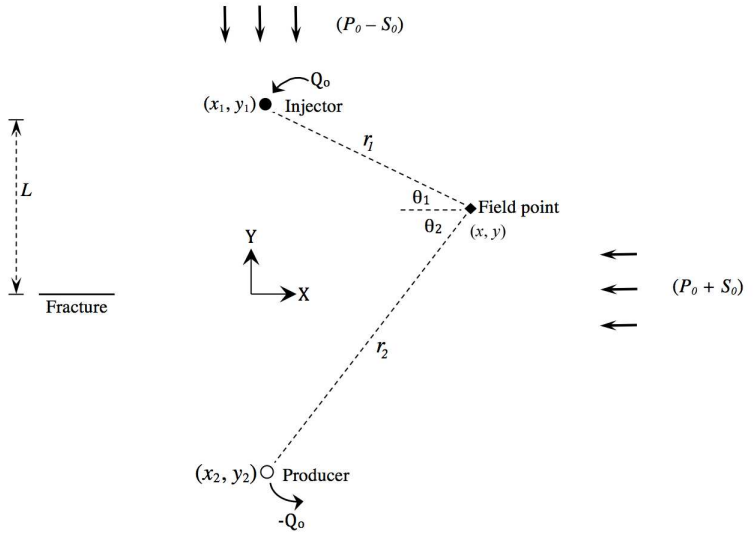

Figure 4.1: Berchenko-Detournay problem [7] with extra annotations

numerical modeling is not done in this work. Rather a new parameter which is a function of fracture toughness was introduced into the stress trajectory equation to approximately account for the effect of rock toughness on the fracture propagation path without recourse to full fracture propagation modeling. The goal is to examine how good of a predictor is the stress trajectory to approximate the fracture propagation direction.

4.2 The Berchenko-Detournay Problem

Consider a hydraulic fracture propagating in a poroelastic medium towards a system of two wells, an injector well injecting fluid at a constant rate Q_o and a producer, withdrawing fluid at the same rate, $-Q_o$ since time $t = 0$ [7]. The fracture, initially propagating equidistant from the two wells, is perpendicular to the far-field compressive minimum principal stress, $P_o - S_o$, where P_o is the mean stress and S_o is the deviatoric stress at infinity (see figure 4.1). The coordinates of the injector and producer are $(0, L)$ and $(0, -L)$, respectively while the hydraulic fracture was propagating along the negative $x - axis$.

Berchenko et. al made the following assumptions about the problem to keep it manageable:

- The internal pressure, p_f of the fracture is constant.
- Effects of leak-off from the fracture is ignored.
- Pore pressure evolution as a result of the injection and pumping activity is negligible while the fracture is still outside the region of influence between the two wells.
- The fracture path is independent of the speed of propagation

With these assumptions, the possible factors influencing the advancing fracture path are (1) the

far field stresses,P_o and S_o and the pore pressure p_o, (2) the injection and pumping rate, Q_o, (3) the poroelastic material constants, (4) the half-distance between the two wells, L, (5) the fracture pressure, p_f and (6) the time, t, as the induced stress field evolves with time due to the pumping and injection.

Berchenko et. al proposed using the stress trajectory to gain some insight into the possible propagation path since fractures generally propagate perpendicularly to the direction of the minimum principal stress or along the direction of the maximum principal stress. This necessitates the need to develop an equation for stress field around the wells which subsequently is then used to produce the stress trajectories.

Berchenko et. al did not provide the derivation of the induced stress field equations but rather gave the final expressions for these quantities. In the next section, the required stress field equations for an unfractured well in a poroelastic medium in a 2D plane strain model is derived for the purpose of completeness and reference.

It should be noted that Berchenko et. al considered tensile forces as positive in their paper, thus the induced stresses were positive while the far field stresses, being compressive, are deemed negative. In this work, we adopted the classical geotechnical convention of compressive stress being positive, thus the induced stresses, being tensile are negative. As such the stress trajectory that will ultimately be developed will follow in the direction of the maximum principal stress rather than the minimum principal stress direction used in Berchenko's paper.

4.2.1 Stress Field Around Injector/ Producer Wells in a Poroelastic medium

4.2.1.1 Displacement and Pore Pressure Field around a Well

To aid the derivations, the equilibrium equation and constitutive equation are written in the polar coordinate system (since we are dealing with a 2D problem). The combination of these two equations will aid in the derivation of one of the field equations (i.e the Navier-type equation for the solid displacement).

The force equilibrium equation is given as

$$\frac{\partial \sigma_{rr}}{\partial r} + \frac{\sigma_{rr} - \sigma_{\theta\theta}}{r} = 0 \tag{4.1}$$

The constitutive equations for the radial and tangential stresses in terms of pore pressure are given as

$$\sigma_{rr} = 2G\varepsilon_{rr} + 2Gp\frac{\nu}{1-2\nu}\varepsilon_{kk} - \alpha p \tag{4.2}$$

$$\sigma_{\theta\theta} = 2G\varepsilon_{\theta\theta} + 2G\frac{\nu}{1-2\nu}\varepsilon_{kk} - \alpha p \tag{4.3}$$

Where the radial, tangential strains and volumetric strains are given respectively by

$$\epsilon_{rr} = \frac{\partial u_r}{\partial r}; \epsilon_{\theta\theta} = \frac{u_r}{r}; \epsilon_{kk} = \frac{\partial u_r}{\partial r} + \frac{u_r}{r} \tag{4.4}$$

We can obtain a partial differential equation for the displacement by substituting (4.2), (4.3),and (4.4) into (4.1) and upon simplification, we obtain

$$\frac{\partial^2 u_r}{\partial r^2} + \frac{1}{r}\frac{\partial u_r}{\partial r} - \frac{u_r}{r^2} = \frac{\eta}{G}\frac{\partial p}{\partial r} \tag{4.5}$$

where

$$\frac{\alpha(1-2\upsilon)}{2(1-\upsilon)} \cdot \frac{1}{G} = \frac{\eta}{G} \tag{4.6}$$

The poroelastic constants in the above expressions have been defined in chapter 2.

The general solution to (4.5) is given by

$$u_r(r,t) = C_1(t)r + C_2(t)\frac{1}{r} + \frac{\eta}{Gr}\int_0^r r' p(r',t)dr' \tag{4.7}$$

Where $C_1(t)$ and $C_2(t)$ are constants of integration.

Since the well diameter is very small compared to the infinite poroelastic medium, the well can be modeled as a line source, as such, as $r \to 0$, the term $C_1(t)r$ in (4.7) also tends to zero. Also, the displacement should be finite and bounded at infinity. Thus as $r \to \infty$, the term $C_2(t)\frac{1}{r}$ in (4.7) also tends to zero. Equation (4.7) reduces to

$$u_r(r,t) = \frac{\eta}{Gr}\int r' p(r',t)dr' \tag{4.8}$$

To obtain $u_r(r,t)$, we need first solve the diffusion equation for pore fluid pressure, $p(r',t)$. The pressure diffusion equation in a poroelastic medium in the absence of fluid body forces is given by

$$\frac{\partial p}{\partial t} - \kappa M\nabla^2 p = -\alpha M\frac{\partial \varepsilon}{\partial t} + M\gamma \tag{4.9}$$

Where γ is the source density and the other parameters defined in Chapter 2.

For an irrotational displacement field in an infinite domain, the pore pressure and displacement change at infinity is zero, thus under such condition, the solid coupling term, $\alpha M\frac{\partial \varepsilon}{\partial t}$ varnishes. The pore pressure diffusion equation uncouples and in the absence of body forces (4.9) reduces to

$$\frac{\partial p}{\partial t} - c\nabla^2 p = \frac{\gamma}{S} \tag{4.10}$$

Where $S = 1/M$ is the uniaxial specific storage coefficient. The solution to (4.10) with a line source of constant continuous injection of fluid volume per unit length, Q_o at the origin from time $t = 0$ is given by Carslaw and Jaeger [14] as

$$p(r,t) = \frac{Q_o}{4\pi(k/\mu)} E_1\left(\frac{r^2}{4ct}\right) \tag{4.11}$$

Where $r^2 = (x - x')^2 + (y - y')^2$,$x' = y' = 0$ is the source location and $E_1$is the exponential integral, $E_1(\xi) = \int_\xi^\infty \frac{e^{-t}}{t} dt$

Thus we can obtain an expression for the radial displacement, $u_r(r,t)$ by substituting (4.11) into (4.8) and upon integration with respect to r'(ranges from 0 to r)

$$u_r(r,t) = \frac{Q_o}{8\pi(k/\mu)} \cdot \frac{\eta}{G} r \left[\frac{4ct}{r^2}\left(1 - exp\left(-\frac{r^2}{4ct}\right)\right) + E_1\left(\frac{r^2}{4ct}\right)\right] \tag{4.12}$$

Note that equations (4.11) and (4.12) is equally applicable to producer wells. The only difference is the change in the flow rate sign from Q_o to $-Q_o$.

Next we introduce some dimensionless parameters with respect to the problem as described in figure (4.1) to aid a general formulation.

We recall that the fracture was initially propagating along the negative $x - axis$ equidistant from the injector and producer whose coordinates are $(X_1, Y_1)$and (X_2, Y_2) respectively.

We define the following dimensionless parameters

$$x = \frac{X}{L}; y = \frac{Y}{L}; x_1 = \frac{X_1}{L}; y_1 = \frac{Y_1}{L}; x_2 = \frac{X_2}{L}; y_2 = \frac{Y_2}{L}; \tau = \frac{4ct}{L^2} \tag{4.13}$$

Where X and Y are the spatial principal coordinates and x, y are the dimensionless spatial coordinates of an arbitrary field point. (x_1, y_1) and (x_2, y_2) are dimensionless injector and producer coordinates respectively.

The radial displacement in (4.12) can be written in terms of the defined dimensionless parameters as

$$u_r(r,\tau) = \frac{Q_o}{8\pi(k/\mu)} \frac{\eta}{G} r \left[\frac{\tau}{r^2}\left(1 - exp\left(-\frac{r^2}{\tau}\right)\right) + E_1\left(\frac{r^2}{\tau}\right)\right] \tag{4.14}$$

And the pore pressure as

$$P(r,\tau) = \frac{Q_o}{4\pi(k/\mu)} E_1\left(\frac{r^2}{\tau}\right) \tag{4.15}$$

The strains induced in the poroelastic medium due to the injector well is obtained by substituting (4.14) into (4.4).

$$\epsilon_{rr}(r,\tau) = \frac{Q_o}{8\pi(k/\mu)} \cdot \frac{\eta}{G}\left[-\frac{\tau}{r^2} + \frac{\tau}{r^2}exp\left(-\frac{r^2}{\tau}\right) + E_1\left(\frac{r^2}{\tau}\right)\right] \tag{4.16}$$

$$\epsilon_{\theta\theta}(r,\tau) = \frac{Q_o}{8\pi(k/\mu)} \cdot \frac{\eta}{G}\left[\frac{\tau}{r^2} - \frac{\tau}{r^2}exp\left(-\frac{r^2}{\tau}\right) + E_1\left(\frac{r^2}{\tau}\right)\right] \tag{4.17}$$

$$\epsilon_{kk}(r,\tau) = \frac{Q_o}{4\pi(k/\mu)} \cdot \frac{\eta}{G}E_1\left(\frac{r^2}{\tau}\right) \tag{4.18}$$

Similarly, the strains induced due to the producer is obtained by merely using $-Q_o$ instead in equations (4.16), (4.17) and (4.18).

The radial and tangential stresses at the field point (x, y) due to the injector is obtained by substituting (4.11), (4.16), (4.17) and (4.18) into (4.2) and (4.3) respectively;

$$\sigma_{rr,inj}(r,\tau) = \frac{Q_o\eta}{4\pi(k/\mu)} \cdot \left[-\frac{\tau}{r_1^2}\left(1 - exp\left(-\frac{r_1^2}{\tau}\right)\right) - E_1\left(\frac{r_1^2}{\tau}\right)\right] \tag{4.19}$$

$$\sigma_{\theta\theta,inj}(r,\tau) = \frac{Q_o\eta}{4\pi(k/\mu)} \cdot \left[\frac{\tau}{r_1^2}\left(1 - exp\left(-\frac{r_1^2}{\tau}\right)\right) - E_1\left(\frac{r_1^2}{\tau}\right)\right] \tag{4.20}$$

Similar expressions are obtained for induced stresses due to the producer by using $-Q_o$ instead in equations (4.19) and (4.20).

4.2.1.2 Stress Functions

We can transform the obtained stresses from polar coordinates to Cartesian coordinates using the stress transformation equations:

$$\sigma_{xx}(x,y,\tau) = \sigma_{rr}(r,\tau)Cos^2\theta + \sigma_{\theta\theta}(r,\tau)Sin^2\theta - 2\sigma_{r\theta}(r,\tau)Sin\theta Cos\theta \tag{4.21}$$

$$\sigma_{yy}(x,y,\tau) = \sigma_{rr}(r,\tau)Sin^2\theta + \sigma_{\theta\theta}(r,\tau)Cos^2\theta + 2\sigma_{r\theta}(r,\tau)Sin\theta Cos\theta \tag{4.22}$$

$$\sigma_{xy}(x,y,\tau) = \left(\sigma_{rr}(r,\tau) - \sigma_{\theta\theta}(r,\tau)\right)Sin\theta Cos\theta + \sigma_{r\theta}(r,\tau)\left(Cos^2\theta - Sin^2\theta\right) \tag{4.23}$$

Bearing in mind that for a plane strain problem, the shear strain, $\epsilon_{r\theta} = 0$ and thus the shear stress,$\sigma_{r\theta} = 2G\varepsilon_{r\theta} = 0$. Thus (4.21) - (4.23) reduces to:

$$\sigma_{xx}(x,y,\tau) = \sigma_{rr}(r,\tau)Cos^2\theta + \sigma_{\theta\theta}(r,\tau)Sin^2\theta \tag{4.24}$$

$$\sigma_{yy}(x,y,\tau) = \sigma_{rr}(r,\tau)Sin^2\theta + \sigma_{\theta\theta}(r,\tau)Cos^2\theta \tag{4.25}$$

$$\sigma_{xy}(x,y,\tau) = \left(\sigma_{rr}(r,\tau) - \sigma_{\theta\theta}(r,\tau)\right) Sin\theta Cos\theta \tag{4.26}$$

After some elementary algebra, the induced horizontal normal stress in Cartesian coordinates, in the $x - direction$ at the field point (x, y) due to the injector is given by:

$$\sigma_{xx}(x,y,\tau)_{,inj} = \frac{Q_o\eta}{4\pi(k/\mu)}\left[\frac{(y-y_1)^2 - (x-x_1)^2}{(y-y_1)^2 + (x-x_1)^2}\left(\frac{1-exp(\psi_1)}{\psi_1}\right) - E_1(\psi_1)\right] \tag{4.27}$$

Where we have used $\psi_1 = \frac{(y-y_1)^2+(x-x_1)^2}{\tau}$,

Following similar approach, we can write the expression for the induced horizontal normal stress in the $x - direction$ at the field point due to the producer $(-Q_o)$ as

$$\sigma_{xx}(x,y,\tau)_{,prod} = -\frac{Q_o\eta}{4\pi(k/\mu)}\left[\frac{(y-y_2)^2 - (x-x_2)^2}{(y-y_2)^2 + (x-x_2)^2}\left(\frac{1-exp\left(-\psi_2\right)}{\psi_2}\right) - E_1(\psi_2)\right] \tag{4.28}$$

Where we have used $\psi_2 = \frac{(y-y_2)^2+(x-x_2)^2}{\tau}$

Similarly, we can obtain the induced horizontal normal stresses due to the injector and the producer in the $y - direction$ following the same approach as above.

These stresses are given as:

$$\sigma_{yy}(x,y,\tau)_{,inj} = \frac{Q_o\eta}{4\pi(k/\mu)}\left[\frac{(y-y_1)^2 - (x-x_1)^2}{(y-y_1)^2 + (x-x_1)^2}\left(\frac{1-exp\left(\psi_1\right)}{\psi_1}\right) + E_1(\psi_1)\right] \tag{4.29}$$

$$\sigma_{yy}(x,y,\tau)_{,prod} = -\frac{Q_o\eta}{4\pi(k/\mu)}\left[\frac{(y-y_2)^2 - (x-x_2)^2}{(y-y_2)^2 + (x-x_2)^2}\left(\frac{1-exp\left(\psi_2\right)}{\psi_2}\right) + E_1(\psi_2)\right] \tag{4.30}$$

The induced shear stresses in the $xy - plane$ for the injector and producer is given as

$$\sigma_{xy}(x,y,\tau)_{,inj} = -\frac{Q_o\eta}{4\pi(k/\mu)} \cdot \left[\frac{2(x-x_1)(y-y_1)}{(y-y_1)^2 + (x-x_1)^2}\left(\frac{1-exp\left(-\psi_1\right)}{\psi_1}\right)\right] \tag{4.31}$$

$$\sigma_{xy}(x,y,\tau)_{,prod} = \frac{Q_o\eta}{4\pi(k/\mu)} \cdot \left[\frac{2(x-x_2)(y-y_2)}{(y-y_2)^2+(x-x_2)^2}\left(\frac{1-exp\,(-\psi_2)}{\psi_2}\right)\right] \tag{4.32}$$

Thus the total induced stresses felt at the field point, (due to injection and pumping) is a superposition of the both induced stresses from the injector and producer wells.

Thus, resultant induced horizontal stresses in the $x-$ and $y-directions$ are given as:

$$\sigma_{xx}(x,y,\tau)_{ind} = \frac{Q_o\eta}{4\pi(k/\mu)}\left[\frac{(y-y_1)^2-(x-x_1)^2}{(y-y_1)^2+(x-x_1)^2}\left(\frac{1-exp\,(-\psi_1)}{\psi_1}\right) - E_1(\psi_1)\right.$$

$$\left. -\frac{(y-y_2)^2-(x-x_2)^2}{(y-y_2)^2+(x-x_2)^2}\left(\frac{1-exp\,(-\psi_2)}{\psi_2}\right) + E_1(\psi_2)\right] \tag{4.33}$$

$$\sigma_{yy}(x,y,\tau)_{ind} = -\frac{Q_o\eta}{4\pi(k/\mu)}\left[\frac{(y-y_1)^2-(x-x_1)^2}{(y-y_1)^2+(x-x_1)^2}\left(\frac{1-exp\,(-\psi_1)}{\psi_1}\right) + E_1(\psi_1)\right.$$

$$\left. -\frac{(y-y_2)^2-(x-x_2)^2}{(y-y_2)^2+(x-x_2)^2}\left(\frac{1-exp\,(-\psi_2)}{\psi_2}\right) - E_1(\psi_2)\right] \tag{4.34}$$

The resultant shear stress in the $xy-plane$ at the field point is given as

$$\sigma_{xy}(x,y,\tau)_{ind} = -\frac{Q_o\eta}{4\pi(k/\mu)}\left[\frac{2(x-x_1)(y-y_1)}{(y-y_1)^2+(x-x_1)^2}\left(\frac{1-exp\,(-\psi_1)}{\psi_1}\right)\right.$$

$$\left. -\frac{2(x-x_2)(y-y_2)}{(y-y_2)^2+(x-x_2)^2}\left(\frac{1-exp\,(-\psi_2)}{\psi 2}\right)\right] \tag{4.35}$$

By introducing a characteristic stress defined by

$$\sigma^* = \frac{Q_o\eta}{4\pi(k/\mu)} \tag{4.36}$$

We can express the induced stresses in their dimensionless forms by normalizing the induced stresses with the characteristic stress. These normalized stresses will be referred to as stress functions , F_{xx}, F_{yy} and F_{xy} for induced horizontal normal stresses in $x-direction$ and$y-direction$, and the induced shear stress in $xy-plane$ respectively.

Thus

$$F_{xx}(x,y,\tau) = \left[\frac{(y-y_1)^2-(x-x_1)^2}{(y-y_1)^2+(x-x_1)^2}\left(\frac{1-exp\,(-\psi_1)}{\psi_1}\right) - E_1(\psi_1)\right.$$

$$\left. -\frac{(y-y_2)^2-(x-x_2)^2}{(y-y_2)^2+(x-x_2)^2}\left(\frac{1-exp\,(-\psi_2)}{\psi_2}\right) + E_1(\psi_2)\right] \tag{4.37}$$

$$F_{yy}(x,y,\tau) = \left[-\frac{(y-y_1)^2-(x-x_1)^2}{(y-y_1)^2+(x-x_1)^2} \left(\frac{1-exp\,(-\psi_1)}{\psi_1} \right) - E_1(\psi_1) \right.$$

$$\left. + \frac{(y-y_2)^2-(x-x_2)^2}{(y-y_2)^2+(x-x_2)^2} \left(\frac{1-exp\,(-\psi_2)}{\psi_2} \right) + E_1(\psi_2) \right] \tag{4.38}$$

$$F_{xy}(x,y,\tau) = \left[-\frac{2(x-x_1)(y-y_1)}{(y-y_1)^2+(x-x_1)^2} \left(\frac{1-exp\,(-\psi_1)}{\psi_1} \right) \right.$$

$$\left. + \frac{2(x-x_2)(y-y_2)}{(y-y_2)^2+(x-x_2)^2} \left(\frac{1-exp\,(-\psi_2)}{\psi 2} \right) \right] \tag{4.39}$$

And the induced stresses can be written as

$$\sigma_{xx}(x,y,\tau)_{ind} = \sigma^* F_{xx}(x,y,\tau) \tag{4.40}$$

$$\sigma_{yy}(x,y,\tau)_{ind} = \sigma^* F_{yy}(x,y\sigma*,\tau) \tag{4.41}$$

$$\sigma_{xy}(x,y,\tau)_{ind} = \sigma^* F_{xy}(x,y,\tau) \tag{4.42}$$

Equations (4.37) - (4.42) are the final set of equations used by Berchenko et. al [7]. As stated earlier, these equations were re-derived for reference and completeness purpose.

Following Berchenko et.al, the stress trajectory equations are provided next.

4.2.1.3 Principal Stresses Direction Equations

Prior to fracture propagation, the total state of stress in the medium is the summation of the far-field stresses and induced stresses due to the wells. Noting that the far field stresses are compressive and the induced stresses are tensile, we can write

$$\sigma_{xx}(x,y,\tau) = \sigma_{xx}(x,y,\tau)_{ind} + P_o + S_o \tag{4.43}$$

$$\sigma_{yy}(x,y,\tau) = \sigma_{yy}(x,y,\tau)_{ind} + P_o - S_o \tag{4.44}$$

$$\sigma_{xy}(x,y,\tau) = \sigma_{xy}(x,y,\tau)_{ind} \tag{4.45}$$

The direction of principal stresses can be predicted using the expression

$$tan2\theta_p = \frac{2\tau_{xy}}{\sigma_{xx} - \sigma_{yy}} \tag{4.46}$$

Where θ_p is the angle the principal stress makes with the positive $x - axis$. Recalling that the maximum principal stress is given by

$$\sigma_1(x, y, \tau) = \frac{\sigma_{yy} + \sigma_{xx}}{2} + \sqrt{\left(\frac{\sigma_{xx} - \sigma_{yy}}{2}\right)^2 + \sigma_{xy}^2} \tag{4.47}$$

Equation (4.46)can be re-written after some elementary algebraic manipulation to give an expression in terms of the maximum compressive principal stress.

$$tan\theta_p = \frac{dy}{dx} = \frac{\sigma_1 - \sigma_{xx}}{\sigma_{xy}} \tag{4.48}$$

Solving this equation gives the maximum principal stress trajectories.

Following Berchenko's approach we can define the following dimensionless parameters for proper analysis of the stress trajectories:

Dimensionless far-field deviatoric stress, $\mathcal{S}$

$$\mathcal{S} = \frac{S_o}{\sigma^*} \tag{4.49}$$

Dimensionless Stress Difference, F_u

$$F_u(x, y, \tau, \mathcal{S}) = \frac{\sigma_{xx} - \sigma_{yy}}{2\sigma*} = \frac{1}{2}\left(F_{xx}(x, y, \tau) - F_{yy}(x, y, \tau)\right) + \mathcal{S} \tag{4.50}$$

Thus, (4.48) can be written in form of the newly defined dimensionless parameters as

$$\frac{dy}{dx} = \frac{-F_u(x, y, \tau; \mathcal{S}) + \sqrt{F_u(x, y, \tau; \mathcal{S})^2 + F_{xy}(x, y, \tau)^2}}{F_{xy}(x, y, \tau)} = f(x, y, \tau; \mathcal{S}) \tag{4.51}$$

Note that equation (4.51) uses the convention, compressive and tensile stresses are positive and negative respectively. This expression is slightly different in signs from that provided in Berchenko et. al equation (15) who used the opposite sign convention. The stress difference (4.50) is also defined differently, with a swapping of the position of $\sigma_{xx}$and σ_{yy}compared to equation (10) in Berchenko. The compressive stress is positive convention was adopted so that the general convention that fracture propagate parallel to the maximum stress field is retained as against Berchenko work that had the fracture propagating parallel to the minimum principal stress due to the sign convention they adopted.

4.2.2 Stress Trajectories Around Wells

Following Berchenko et al., the maximum principal stress trajectories around the injector-producer system are examined. The differential equation (4.51) is solved numerically using the computational software, Mathematica and the corresponding plots generated. It should be noted that the distance between the wells in these plots have been normalized (see (4.13)) and as such the spatial distances are dimensionless.

Figure 4.2 shows 1 injector - 1 producer system for various values of τ and $\mathcal{S}$. The fracture predicted path is indicated by the magenta line The following qualitative observations can be made from the stress field plots:

1. At very early times, the maximum principal stress field is relatively unperturbed for large values of the dimensionless deviatoric stress parameter, $\mathcal{S}-$ the ratio of the far-field deviatoric stress, S_o, to the characteristic stress, $\sigma*$, which is a function of the rock properties as well as the flow rate.

2. As injection and production continues for some extended time, we notice appreciable perturbation of the stress field around the wells. This perturbation is more pronounced at smaller values $\mathcal{S}$.

3. An "attraction basin" is developed around the injector at longer times, while the producer develops a repulsive zone. A fracture propagating within the attraction zone may end up in the injector well.

4. At values of $\mathcal{S} > 1$, the fracture is deviated but does not end up in the injector. χ

Berchenko et. al defined the dimensionless toughness parameter as $\chi = K_{\mathrm{Ic}}/(\sigma^*\sqrt{l_o})$, where K_{Ic} is the rock's toughness,l_o is the initial fracture half length before propagation and σ^* is the characteristic stress. χ is a measure of the ratio of the net pressure in the fracture to the characteristic stress σ^*.They showed that as long as χ is small (say less than 0.1 as shown in figure 4.3(a)), the stress trajectory does produce a very good estimate for the fracture propagation path by comparing the stress trajectory prediction with the full-scale numerical modeling of the fracture propagation path. They also stated that as long as the χ is small, fracture deviation and attraction is primarily controlled by two dimensionless groups, $\mathcal{S} = S_o/\sigma^*$ which is the ratio of the far field stress deviator and the characteristic stress, σ^* and dimensionless time, $\tau = 4ct/L^2$. In the general case when the dimensionless toughness parameter is not small, the solution depends on eight dimensionless parameters in all and a full numerical fracture propagation modeling must be pursued to predict the fracture path.

Figure 4.2: Maximum principal stress trajectories around an injector-producer system at various values of τ and $\mathcal{S}$

In the next section, a new perturbation parameter and a dimensionless toughness parameter modifier, Υ which when incorporated into the standard stress trajectory equation, could help approximate the actual fracture path without recourse to a full numerical modeling of the fracture

propagation. This implies that the fracture path, perhaps, may be controlled by three dimensionless parameters instead of eight, that is, the two dimensionless groups earlier described, $\mathcal{S}$ and τ, and a new parameter which is a dimensionless toughness parameter modifier, Υ.

4.2.3 The Modified Stress Trajectory Equation

Here we introduce the *dimensionless toughness parameter modifier,* Υ. Berchenko provided the following expression for the dimensionless toughness parameter χ

$$\chi = \frac{K_{\mathrm{Ic}}}{\sqrt{l_o}\sigma*} \tag{4.52}$$

where K_{Ic} is the poroelastic media toughness, l_o is the initial fracture length prior to propagation and $\sigma*$ is the characteristic stress as defined previously.

The *dimensionless toughness parameter modifier*, Υ is given by

$$\Upsilon = Exp\left(-\vartheta\sqrt{\chi}\right) \tag{4.53}$$

where ϑ is the *dimensionless toughness fitting parameter* . Equation (4.53) was obtained by fitting the dimensionless toughness parameter values of the full numerical solution by Berchenko and Detournay to a scale ranging from 0 to 1 using an exponential function. For the Berchenko-Detournay problem considered, the *dimensionless toughness fitting parameter,* ϑ was determined to be ≈ 0.2539.

By incorporating the modified dimensionless toughness parameter into the maximum principal stress direction equation, we can approximate the fracture path for any value of toughness, without a recourse to full scale fracture propagation modeling.

Thus a modified principal stress trajectory equation that can provide an approximate fracture path is given by

$$\frac{dy}{dx} = \Upsilon\frac{\sigma_1 - \sigma_{xx}}{\sigma_{xy}} \tag{4.54}$$

It is worth noting that the value of Υ ranges from 0 to 1. When $\Upsilon \to 0$, which implies high dimensionless toughness values, the stress trajectory is less perturbed and thus the fracture tend to continue on a straight ahead course. When $\Upsilon \to 1$, the stress trajectory equation tends to the standard principal stress trajectory equation which produces good fracture path estimates for small toughness values.

A plot showing the variation of predicted fracture path for an injector-producer system at $\tau = 1$ and $\mathcal{S} = 0.5$ for various values of the modified dimensionless toughness parameter, Υ is shown in Figure 4.3(b). The red and blue dots indicates the injector and producer respectively.

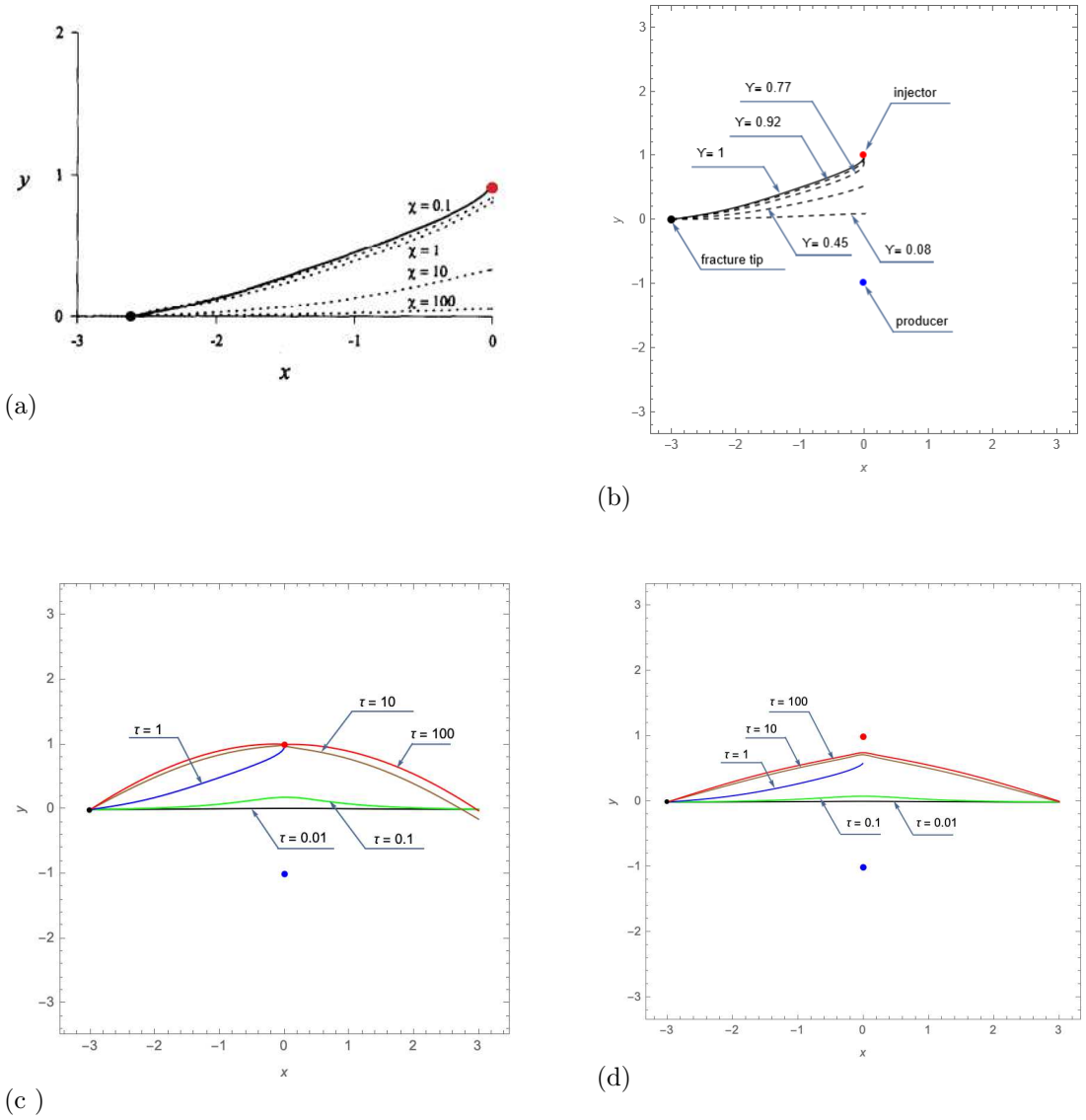

Figure 4.3: Approximated fracture paths at $\mathcal{S} = 0.5$ for various values $\tau$and χ or Υ:(a) From Fig. 12, Berchenko et. al [7] comparing numerical fracture path prediction (dotted curves) and the stress trajectory (continuous line) for $\mathcal{S} = 0.5$ at $\tau = 1$ ($\chi = 0.1, 1, 10, 100$) (b) Predicted fracture path for various values of Υ at $\tau = 1$ and $\mathcal{S} = 0.5$. Υ values were calculated using $\chi = 0.1, 1, 10, 100$ from Berchenko et. al [7] (c)-(d) Predicted fracture path, $\mathcal{S} = 0.5$ at various times $\tau = 0.01, 0.1, 1, 10, 100$ for $\Upsilon = 1$ and $\Upsilon = 0.5$ respectively.

The fracture tip is represented by the black dot and it is at the point $(-3, 0)$. The lines emanating from this point are the predicted stress trajectory that the propagating fracture would follow for the various toughness values using the modified stress trajectory equation (4.54). A visual comparison of 4.3(b) and Berchenko's numerical solution as shown in 4.3(a) shows great similarity. The Υ values used in the plot are calculated using (4.53) with $\chi = 0.1, 1, 10, 100$ as used in Berchenko's paper. While it was intended that a comparison with a numerical solution will be carried out, unfortunately, that piece of exercise will not be captured in this thesis but will be carried out and published in a paper at a future date.

Figure 4.3(c) shows various predicted fracture path for a fracture whose tip is at the point $(-3, 0)$ for various times when $\Upsilon = 1$ and $\mathcal{S} = 0.5$. Note that $\Upsilon = 1$ is synonymous with zero toughness and as such gives same plot as the standard maximum principal stress trajectory equation. As expected, we observe the fracture path to continue on a straight course at early times ($\tau = 0.01$) and gradually deviated as injection and production continues. At times greater than $\tau = 1$, the fracture get ends up in the injector well. Similarly, Figure 4.3(d) shows various predicted fracture path for a fracture whose tip is at the point $(-3, 0)$ for various times when $\Upsilon = 0.5$ and $\mathcal{S} = 0.5$. We observe that although the fracture gets deviated at late times, the fracture does not end up in the injector well because the influence of the fracture toughness is greater than the induced poroelastic stress changes.

In conclusion, the Berchenko-Detournay problem was revisited with additional stress trajectory plots provided to give pictorial view of the influence of the various dimensionless groups namely, $\mathcal{S}$ and τ . A new dimensionless toughness parameter modifier and a modified maximum principal stress direction equation were introduced with the goal of predicting fracture propagation path without explicitly modeling the fracture propagation.

Chapter 5

Stress Field Around a Fractured Producer Well

5.1 Introduction

The majority of wells, in recent years, used for production purposes are hydraulically fractured. The advancement in fracturing technologies in recent times have influenced many oil and gas field operators to conclude that older generation wells which are mostly vertical wells, may have been understimulated and as such they could be good candidates for refracturing in order to recover stranded hydrocarbon reserve. One major factor operators seek to understand is the stress state in a reservoir after it has been producing for some extended period of time. Of particular interest is the stress field re-orientation and possible principal stresses reversals (switching of the directions of the principal stresses around the fracture). Should a stress reversal occur, a new refracture will propagate perpendicular to the old fracture, thereby increasing the likelihood of the new fracture contacting less depleted segments of the reservoir.

In this chapter, the equations and solutions for the induced stress fields around a producer well are developed. The induced stress fields solutions were derived using previous transient pressure solutions by Sarvaramini and Garagash[47]. Stress trajectories are employed to visualize the stress perturbations as well as the extent of stress reorientation. The variation of the extent of the orthogonal segment of the theoretical refracture length as well as the conditions for which such stress reversals take place are presented. The problem solved here is modeled in 2D plane strain.

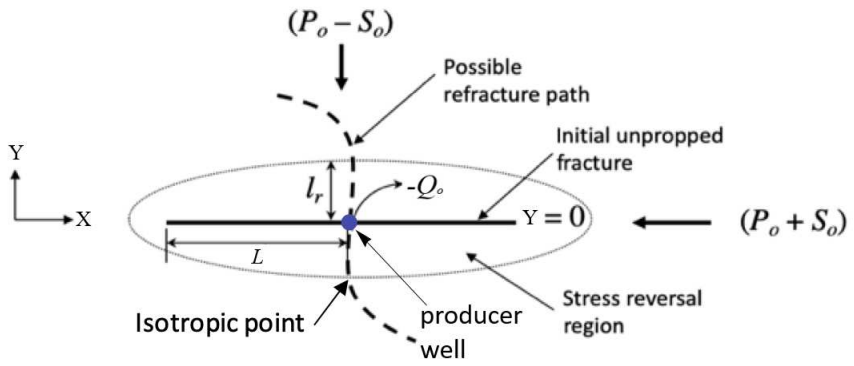

Figure 5.1: A fractured producer well in a non-hydrostatic poroelastic medium

5.2 Problem Description

We consider an unpropped fractured producer well flowing at a constant rate $-Q_o$ in a poroelastic reservoir with ambient an pore pressure p_o. The fracture, of length $2L$ perpendicular to the minimum compressive far field stress $P_o - S_o$, where P_o is the mean stress and S_o is the stress deviator at infinity. Here we take the compressive stresses as positive. The poroelastic medium is homogeneous and the crack itself is modeled in plane strain (infinite height). The fracture is highly conductive to fluid compared to the formation. Fluid flow in the fracture is not modeled. This is a reasonable assumption for an unpropped producer well because the crack volume is small compared to the leak-in volume and the fluid pressure in the fracture is less than the pressure required to advance the crack.

A schematic of the problem description is given in figure 5.1.

5.2.1 Governing Equations and Boundary Integral Representation

To determined the induced stresses around the fracture due to fluid production, we need to first quantify the transient pressure field around the fracture. This can be achieved by solving the pore pressure diffusion equation using the concept of distributed sources over the fracture locus. We recall the pore pressure diffusion equation in a poroelastic medium in the absence of fluid body forces is given by [16]

$$\frac{\partial p}{\partial t} - \kappa M \nabla^2 p = -\alpha M \frac{\partial \varepsilon}{\partial t} + M\gamma \tag{5.1}$$

Where γ is the source density, $\kappa = k/\mu$ is the mobility coefficient, k is the intrinsic matrix permeability, μ is the dynamic fluid viscosity, M is the Biot's Modulus, α is Biot's coefficient and ϵ is the volumetric strain.

As stated in chapter 4, for an irrotational displacement field in an infinite domain, the pore

pressure and displacement change at infinity is zero, thus under such condition, the solid coupling term varnishes [16, 60] . Thus, the pore pressure diffusion equation uncouples and for a plane strain problem, (5.1) reduces to

$$\frac{\partial p}{\partial t} - c\nabla^2 p = \frac{\gamma}{S} \tag{5.2}$$

The point source solution to (5.2) subject to a source density, $\gamma = g\delta(r - r^{'})\delta(t - t^{'})$, has been given by Carslaw and Jaeger [14]:

$$p^{si}(R,t) = \frac{g(r^{'},t')}{4\pi cS(t-t^{'})} exp\left(-\frac{|r-r^{'}|^2}{4c(t-t^{'})}\right) \tag{5.3}$$

with $|r - r^{'}|^2 = (X - X^{'})^2 + (Y - Y^{'})^2$, X and Y are the spatial coordinates of an arbitrary field point while $X^{'}$ and $Y^{'}$ are the coordinate of the point source, g is the strength of the Dirac delta function and p^{si} is the instantaneous fluid source solution to (5.2).

We can obtain an expression for the pore pressure field around the crack by distributing the instantaneous sources $p^{si}(X,t)$ over the crack length ($-L \leq X^{'} \leq L, Y^{'} = 0$). Integrating in space and time gives the boundary integral equation for the pressure field [47].

$$p(X,Y,t) - p_o = \int_0^t \int_{-L}^{L} \frac{g(X^{'},t^{'})}{4\pi cS(t-t^{'})} exp\left(-\frac{(X-X^{'})^2 + Y^2}{4c(t-t^{'})}\right) dX^{'}dt^{'} \tag{5.4}$$

where p_o is the formation pore pressure and g takes on the meaning of fluid leak-in rate (rate at which fluid flow into the fracture).

To obtain the full solution for (5.4), the volume balance expression that relates the fluid leak-in rate,g to the overall flowrate must be analyzed.

The volume balance equation is given as

$$\text{Total fluid produced},V(t) = \text{Total fluid leak-in},V_{leak-in} \tag{5.5}$$

Equation (5.5) assumes that the crack volume is negligible which is a good approximation for unpropped cracks around a well as those encountered in a hydrocarbon reservoirs.

Solving (5.4) together with (5.5) for the leak-in rate, g, will enable the formulation of the expressions required to model the induced stress field around the fracture.

5.3 Transient Pressure Drop in the Fracture

The pressure transient and leak-in solutions described in this section is attributed to Sarvaramini and Garagash[47] who derived the relevant transient and asymptotic solutions for the injector well. Only a sign change is required to model similar parameters in the production case. Their

solution is however reproduced here as it forms the foundation for the induced stresses solution later constructed.

5.3.1 Auxiliary Problem: Step Pressure Drop in a Crack

Following Detournay and Cheng[23] and Sarvaramini and Garagash[47], the solution to (5.4) for a crack at $Y = Y^{'} = 0, |X^{'}| < L$ can be facilitated by first solving an auxiliary problem in which the crack is assumed to be at a constant pressure and the crack is then subjected to a sudden step pressure decrease of magnitude $p(X,t) - p_o = -\Delta p$.

We can define the following dimensionless parameters to aid the transformation of (5.4) to a non-dimensional form;

$$x = \frac{X}{L}, \quad y = \frac{Y}{L}, \quad \tau = \frac{4ct}{L^2}, \quad \psi(X^{'}, \tau^{'}) = \frac{g(X^{'}, t^{'})L}{4cS\Delta p} \tag{5.6}$$

Equation (5.4) can now be written in dimensionless as

$$-1 = \frac{1}{\pi} \int_0^{\tau} \int_{-1}^{1} \psi(x^{'}, \tau^{'}) \frac{1}{\tau - \tau^{'}} exp\left(-\frac{|x - x^{'}|}{\tau - \tau^{'}}\right) dx^{'} d\tau^{'} \tag{5.7}$$

Applying Laplace Transform to (5.7) produces

$$-\frac{1}{s} = \frac{2}{\pi} \int_{-1}^{1} \psi(x^{'}, s) K_o\left(2\sqrt{s}|x - x^{'}|\right) dx^{'} \tag{5.8}$$

where K_o is the modified Bessel function of the second kind, s is the Laplace transform parameter and $\psi(x^{'}, s)$ is the Laplace image of $\psi(x', \tau')$.

The numerical solution to (5.8) is obtained in the Laplace space using boundary element approach [40] and subsequently inverted to the time domain using the Stehfest algorithm[56] (see chapter 3 and Appendix B for details). The small and large time asymptotes of equation (5.8) has been provided by Sarvaramini and Garagash[47] for the injection case with only a sign change required for the production case. Figure (5.2) shows the numerical solution (dotted plots) as well as the small and large time asymptotes (line plots) of the dimensionless leak-in parameter, $\psi(x^{'}, \tau)$ after Sarvaramini and Garagash [47].

5.3.2 Cummulative Leak-In Volume Into The Crack

Following Sarvaramini and Garagash [47], the leak-in volume due to the auxiliary problem is given by

$$V_{leak-in}^{aux}(t) = -L^2 S \Phi(4ct/L^2) \tag{5.9}$$

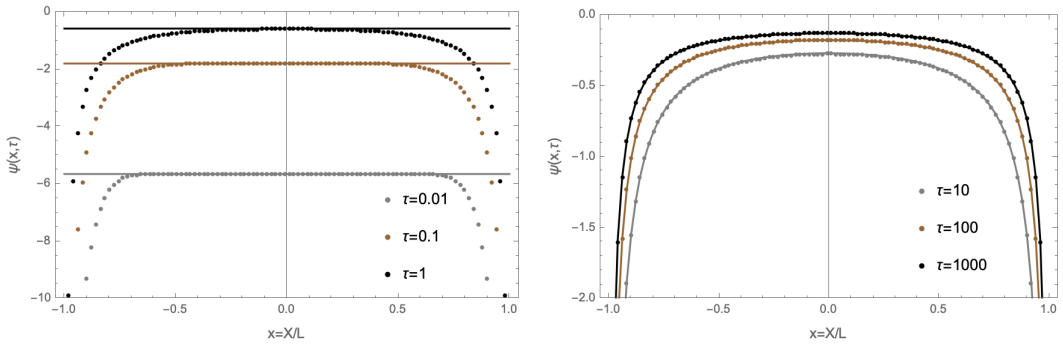

(a) (b)

Figure 5.2: Numerical solution for the normalized leak-in rate in the auxiliary problem compared to (a) the small time and (b) large time times asymptotes after [47]

where $\Phi(\tau)$ is the normalized cumulative leak-in volume given by the expression

$$\Phi(\tau) = \int_0^{\tau} \int_{-1}^{1} \psi(x,\tau) dx d\tau \tag{5.10}$$

The small and large time asymptotes of the normalized leak-in volume for the injector case has been obtained by Sarvaramini and Garagash [47] and Detournay and Cheng[22]. The Producer case is obtained simply by a change of sign of the dimensionless leak-in, $\psi(x,\tau)$ in the solution given in [47] .

5.3.3 Transient Pressure Drop in the Crack Due to Constant Production Rate

Following Sarvaramini and Garagash [47] and Detournay and Cheng[22], the fracture responses such as the transient depressurization and induced stresses due to production can be obtained from the auxiliary solution using the Duhamel's principle. For a transient pressure drop, $p = p(t)$, a fracture response $\mathcal{F}$, can be obtained by convolution such that

$$\mathcal{F}(X,Y,t) = \int_0^t \mathcal{F}^{aux}(X,Y,t-t^{'}) \frac{dp}{dt'} dt' \tag{5.11}$$

where $\mathcal{F}^{aux}$ is the fracture response in the auxiliary problem. Applying (5.11) to the volume balance (5.5),

$$-Q_0 t = \int_0^t V^{aux}_{leak-in}(t-t^{'}) \frac{dp}{dt'} dt' \tag{5.12}$$

Where $V(t) = -Q_0 t$, $t \geq 0$, and $-Q_0$ is the constant production rate per unit length. Using (5.9) and (5.11) we can write

$$-Q_0 t = -L^2 S \int_0^t \Phi\left(\frac{4c(t-t')}{L^2}\right) \frac{dp}{dt'} dt' \tag{5.13}$$

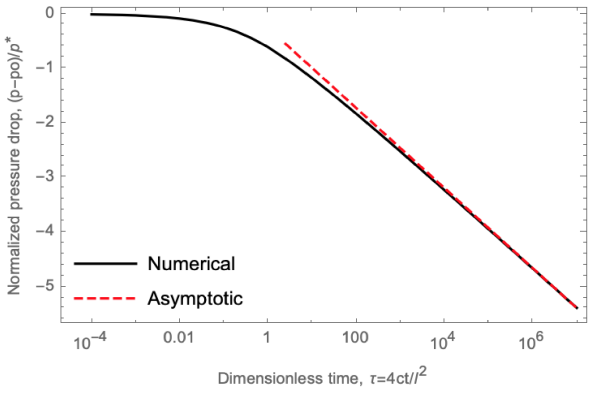

Figure 5.3: Normalized transient net pressure drop in the crack due to fluid production with its long time asymptote after [47].

Equation (5.13) can be solved to obtain the transient pressure drop, $p(t)$ in the crack. By defining the dimensionless parameters,

$$p^* = \frac{Q_0}{4cS}, \quad \Pi = \frac{p - p_o}{p^*} \tag{5.14}$$

equation (5.13) can be written in a dimensionless form as follows

$$\tau = \int_0^\tau \Phi\left(\tau - \tau'\right) \frac{d\Pi}{d\tau'} d\tau' \tag{5.15}$$

Taking the Laplace transform of (5.15) and solving for the dimensionless pressure term, we have

$$\hat{\Pi}(s) = \frac{1}{s^3 \hat{\Phi}(s)} \tag{5.16}$$

The obtained expression can be inverted back to time domain using Stehfest algorithm. Equation (5.16) is subsequently used in the formulation of the expressions for the induced stresses in the poroelastic medium.

In addition to the numerical solution for the transient pressure, Sarvaramini and Garagash [47] also obtained the large-time asymptote for the transient pressure decline given by the expression (in dimensionless form)

$$p(\tau) = -\frac{1}{\pi}\left(ln(4\tau) - \gamma\right) \tag{5.17}$$

where γ is the Euler gamma constant with a value of ≈ 0.5772. A plot of the normalized transient pressure drop with its large time asymptote[47] is shown in figure 5.3.

5.4 Induced Stresses Around A Fractured Producer Due to Constant Fluid Production

In this section, the expressions for the induced stresses around a fractured producer with a constant production rate using the corresponding solution for the transient depressurization in section 5.3 is developed.

First, we formulate expressions for the induced stresses in the auxiliary problem of a step pressure decrease using the instantaneous fluid source Green's functions for poroelastic stresses [16].

$$\sigma_{ij}^{aux}(X,Y,t) = \frac{1}{\pi}\frac{\eta}{S}\int_0^t \int_{-L}^{L} \frac{g^{aux}(X^{'},t^{'})}{r^2}\left[(\delta_{ij} - 2r_{,i}r_{,j})\left(1 - e^{-\varphi^2}\right) - 2\left(\delta_{ij} - r_{,i}r_{,j}\right)\varphi^2 e^{-\varphi^2}\right] dx'dt' \tag{5.18}$$

where $g^{aux}(X,t)$ is the leak-in rate solution in the auxiliary problem, given in the normalized form (5.6) and in figure5.2, $\varphi^2 = \frac{r^2}{4c(t-t')}$, $r = |\mathbf{X} - \mathbf{X}'| = \sqrt{(X-X')^2 + Y^2}$,$r_{,i} = \frac{\partial r}{\partial \mathbf{X}_i} = \frac{X_i - X_i'}{r}$; $\mathbf{X}, \mathbf{X}'$ are spacial coordinates vectors, i and j ranges from 1 to 2 .

The induced stresses due to continuous production of fluid at a constant rate, $-Q_o$ can be obtained using the Duhamel's principle (5.11), such that

$$\sigma_{ij}^{ind}(X,Y,t) = \int_0^t \sigma_{ij}^{aux}(X,Y,t-t^{'})\frac{dp}{dt'}dt' \tag{5.19}$$

where $p(t)$ is the corresponding transient solution for the pressure in the crack as provided in section 5.3, Figure 5.3. Since the transient pressure solution has previously being obtained in the Laplace space in (5.16), it is convenient to transform (5.19) into the Laplace space before inverting back to time domain.

We can re-write (5.19) in dimensionless form after taking its Laplace transform. Recalling that $\Pi = (p - p_o)/p^* = (4cS(p-p_o)/Q_o)$ and defining $\hat{\bar{\sigma}}_{ij}^{ind} = \hat{\sigma}_{ij}^{ind}/\sigma^*$, equation (5.19) becomes

$$\hat{\bar{\sigma}}_{ij}^{ind}(x,y,s) = \hat{\sigma}_{ij}^{aux}(x,y,s)s\hat{\Pi}(s) \tag{5.20}$$

Where σ^*, is the characteristic stress given by

$$\sigma^* = \eta p^* = \frac{\eta Q_o}{4cS} \tag{5.21}$$

and η, is the poroelastic stress coefficient given by

$$\eta = \frac{\alpha(1-2\upsilon)}{2(1-\upsilon)} \tag{5.22}$$

The components of $\hat{\sigma}_{ij}^{aux}(x, y, s)$ in Laplace space are given in Appendix B. The $\hat{}$ signifies the Laplace transform of the parameter under the hat.

Inverting (5.20) back into the time domain using Stehfest algorithm gives the required dimensionless induced stresses in the medium due to constant rate of volumetric production. The obtained results can then be used to model the stress field around the fractured producer.

Figure 5.4(a) - (b) shows the evolution of the normalized induced normal stresses, $\bar{\sigma}_{xx}^{ind} = \sigma_{xx}^{ind}/\sigma^*$ and $\bar{\sigma}_{yy}^{ind} = \sigma_{yy}^{ind}/\sigma^*$ with time along the along the crack centerline ($x = 0, |y| < 10$). We notice that $\bar{\sigma}_{yy}^{ind}$ stays tensile while $\bar{\sigma}_{xx}^{ind}$ switches sign from tensile to compressive and back to tensile at early times. At large times, $\bar{\sigma}_{xx}^{ind}$ remains tensile. 5.4(c)-(d) shows the evolution of the normalized induced shear stresses, $\bar{\sigma}_{xy}^{ind}$ along lines $x = -1$ and $x = 1$ respectively. We note that σ_{xy}^{ind} is zero at these points when $y = 0$. 5.4(e), shows the magnitude of $\bar{\sigma}_{xx}^{ind}$ and $\bar{\sigma}_{yy}^{ind}$ increase with time with their large time asymptote at the middle of the crack, $x = y = 0$. 5.4(f) shows the induced stress difference between the horizontal normal stresses. We note that at around $\tau \approx 10$, the stress difference reaches a maximum in the middle of the crack. A look at figure 5.3 shows that the production well transitioned into a pseudo steady state at about $\tau \gtrsim 10$. It is therefore not surprising to see a similar behaviour in the induced stress field as both pore pressure and stresses are usually coupled in a reservoir system. The magnitude of asymptotic induced dimensionless stress difference was computed to be $2/\pi$. The derivation of the asymptotic expression is found in Appendix B. Although the magnitude of these horizontal stresses change as production continues, the difference in their values at large times remains constant.

5.5 Modeling Stress Trajectories Around a Producer Well

In this section, the stress trajectories around a fractured producer well in a non-hydrostatic stress field is examined. Using the induced stress results obtained in section 5.4, the maximum principal stress trajectories can be constructed following Berchenko and Detournay [8] approach. It should be noted that Berchenko et. al considered the stress trajectories around a pair of unfractured producer-injector system while Siebrits et al [53] considered both unbounded (infinite height) and bounded fractured producer well. Here, a fractured producer well in plane strain (infinite height) is studied as done by Siebrits et al [53] . The main contribution here is to quantify the extent of stress reorientation based on production time and far-field stress deviator as well as provide explanation for the seemingly discrepancies between field measurement of refracture azimuth and predicted path.

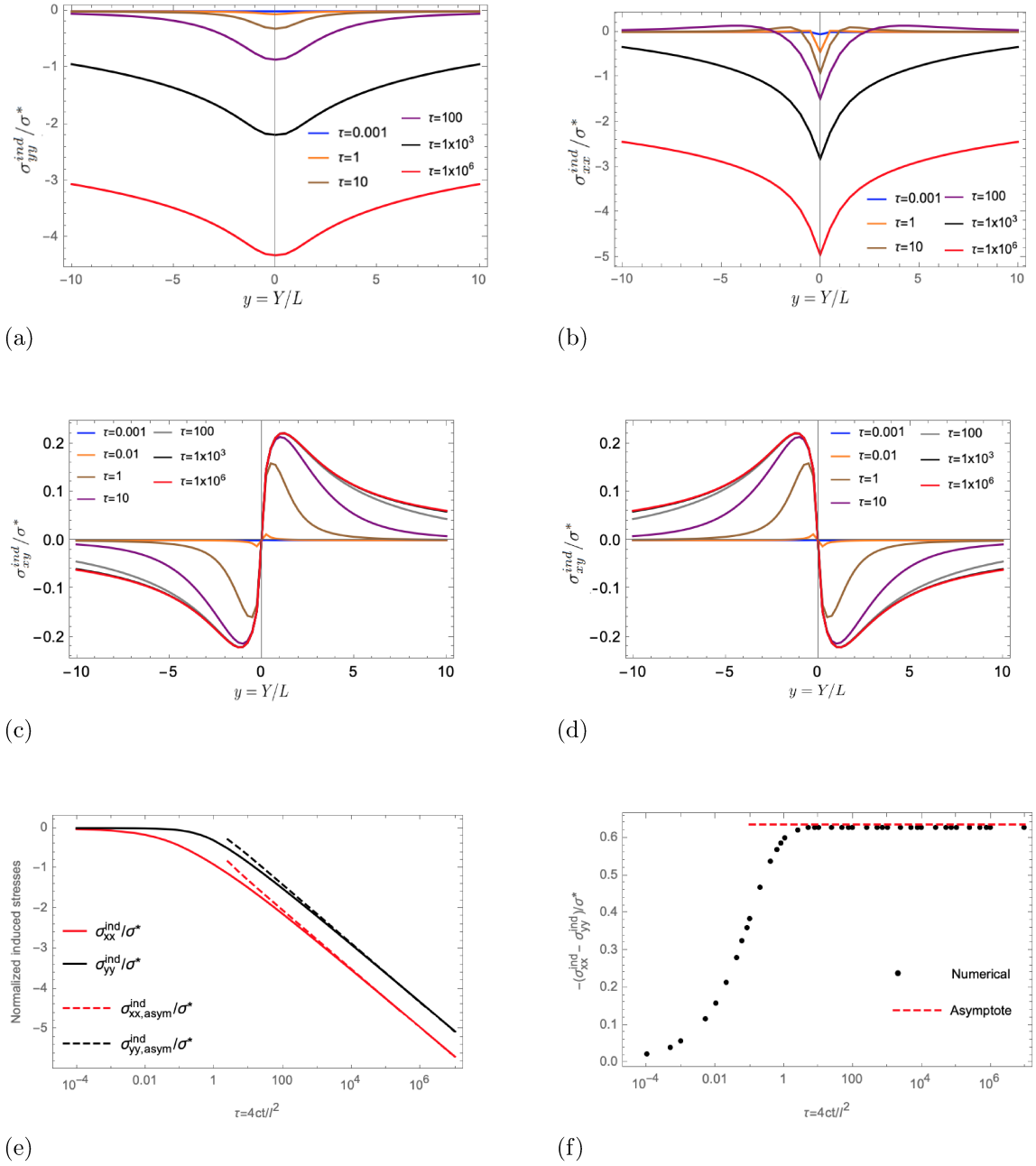

Figure 5.4: Plots for various normalized induced stresses: (a)-(b) Evolution of $\bar{\sigma}_{yy}^{ind}$ and $\bar{\sigma}_{xx}^{ind}$ with time at $x = 0$ and $-10 \leq y \leq 10$;(c)-(d) Evolution of $\bar{\sigma}_{xy}^{ind}$with time along $-10 \leq y \leq 10$ for lines passing through $x = -1$ and $x = 1$ respectively. (e) Evolution of $\bar{\sigma}_{yy}^{ind}$ and $\bar{\sigma}_{xx}^{ind}$ with time at $x = 0$ with their long term asymptotes (f) stress difference between $\bar{\sigma}_{yy}^{ind}$ and $\bar{\sigma}_{xx}^{ind}$ over time. This has implications for extent for stress reversal.

5.5.1 Stress Trajectory Equation

We can use the induced stresses to quantify the perturbed principal stress directions due to the production activity and generate the maximum principal stress field trajectories around such the fracture as follows:

We consider the fractured well as shown in Figure (5.1), the total state of stress in the medium prior to well refracturing is the summation of far-field stresses and the induced stresses which are given by

$$\sigma_{xx}(x,y,\tau) = \sigma_{xx}^{ind}(x,y,\tau) + P_o + S_o \tag{5.23}$$

$$\sigma_{yy}(x,y,\tau) = \sigma_{yy}^{ind}(x,y,\tau) + P_o - S_o \tag{5.24}$$

$$\sigma_{xy}(x,y,\tau) = \sigma_{xy}^{ind}(x,y,\tau) \tag{5.25}$$

whereP_o and S_o are the far field mean stress and the far-field deviatoric stress respectively. The induced stress components $\sigma_{xx}^{ind}(x,y,\tau)$, $\sigma_{yy}^{ind}(x,y,\tau)$ and $\sigma_{xy}^{ind}(x,y,\tau)$ are obtained by inverting (5.20) back to time domain.

As done in chapter 4, sub-subsection 4.2.1.3, we can write the equation for the maximum principal stress field trajectory using the following dimensionless parameters;

Dimensionless far-field deviatoric stress, $\mathcal{S}$

$$\mathcal{S} = \frac{S_o}{\sigma^*} \tag{5.26}$$

Dimensionless Stress Difference, F_u

$$F_u(x,y,\tau,\mathcal{S}) = \frac{\sigma_{xx} - \sigma_{yy}}{2\sigma*} = \frac{1}{2}\left(\bar{\sigma}_{xx}^{ind}(x,y,\tau) - \bar{\sigma}_{yy}^{ind}(x,y,\tau)\right) + \mathcal{S} \tag{5.27}$$

The maximum principal stress equation is given by

$$\frac{dy}{dx} = \frac{-F_u(x,y,\tau;\mathcal{S}) + \sqrt{F_u(x,y,\tau;\mathcal{S})^2 + \bar{\sigma}_{xy}^{ind}(x,y,\tau)^2}}{\bar{\sigma}_{xy}^{ind}(x,y,\tau)} \tag{5.28}$$

5.5.2 Stress-reversal Around the Producer Well

Figure 5.5(a)-(i) shows the maximum principal stress trajectories around the fractured producer well for dimensionless time $\tau = 0.01, 1, 10$ and for varying stress deviator, $\mathcal{S} = 0.35, 0.2, 0.1$. The stress field is most perturbed as $\mathcal{S} \to 0$ (isotropic) and the opposite is observed with increasing

value of $\mathcal{S}$. We also note that the stress field is increasingly perturbed with increasing production time, τ. A 90^ore-orientation (the stress reversal of the maximum and the minimum principal stresses directions) is not observed in all plots even at higher production times because there are certain conditions that need must be met for such a reversal to occur. It is well established that fluid production leads to overall decrease in the total reservoir (horizontal) stresses [28, 63, 1]. From 5.4(a)-(b) we observe that the magnitude of induced horizontal stresses, $\bar{\sigma}_{xx}^{ind}$ and $\bar{\sigma}_{yy}^{ind}$ are not uniform with time and distance from the fracture − that is , the magnitude of $\bar{\sigma}_{xx}^{ind}$ is increasing at a faster rate than $\bar{\sigma}_{yy}^{ind}$. This implies the total horizontal stress, in the direction of the maximum principal stress, σ_{xx} given by (5.23), is reducing at a faster rate than σ_{yy} given by (5.24). If production continues and the stress perturbation region grows, a time comes when σ_{xx} becomes smaller than σ_{yy} in the neighborhood of the fracture, thereby causing a reversal of the principal stress field around the fracture [28, 63, 1]. This reversal however is within an elliptical circumference around the fracture and it is bounded by the isotropic points - points where both the minimum and the maximum horizontal stresses are equal and shear stress is zero. These points form a locus along the $y - axis$ and it's evolving length is denoted as l_r as shown in Figure 5.1. A refracture, theoretically speaking, is therefore expected to propagate perpendicular to the initial fracture until it reaches the boundary of the stress reversal region (delineated on the $y-axis$ by isotropic points) after which the refracture is expected to re-orient itself gradually to align once again parallel to the initial fracture. The potential refracture length extent is dependent on both production time and the far-field stress deviator [53].

Figure 5.6(a) shows the evolution of the theoretical orthogonal segment of the refracture half-length, l_r, with dimensionless time for $\mathcal{S} = 0.01$. We observed that for a purely poroelastic consideration in an infinite medium, this length (l_r), approaches a maximum value of ≈ 0.577 from $\tau \gtrsim 10$ as shown by the plateau of the curve in the figure. This limiting value of l_r for a medium whose stress state is nearly isotropic, is in agreement with previous investigation by Siebrits et al [53] who considered a bounded fracture height and gave the asymptotic value for l_r as 0.58 of the initial fracture half length, L.

A plot of the variation of l_r with the dimensionless stress deviator,$\mathcal{S}$ is shown in figure 5.6(b) for $\tau = 10$. It is observed that from $\mathcal{S} \gtrsim 0.31$, no stress reversal (90-degree re-orientation) is observed anywhere along the crack, though the stress field is still being perturbed at intermediate to large times. This observation can have significant implications in refracturing practice. In many hydraulic fracturing modeling, it is often assumed that the far-field horizontal stress state in the reservoir is nearly isotropic, that is $\mathcal{S} \approx 0$. With this assumption, one would expect that during a refracture exercise, the new fracture should propagate orthogonal to the initial fracture at least at the initial stage before realigning itself parallel to the old fracture. Many field

observations however seems to suggest a wide range of initial refracture angles (some published data put the angle at between $0 - 90$ degrees using tiltmeter data [63, 52, 45, 42]). A couple of plausible explanations could be provided for this variance. From figure 5.6(b) we observe that there will be no 90-degree re-orientation for $\mathcal{S} \gtrsim 0.31$ irrespective of production time. The dimensionless parameter, $\mathcal{S}$, which is a function of the far-field stress deviator, S_o may actually be significant, contrary to the common assumption that the compressive stresses in the medium is nearly uniform both in the x and y directions (i.e $\mathcal{S} \approx 0$). Such assumption may be oversimplifying and might be helpful to have accurate in-situ stress measurements prior to placing wells or attempting refracturing. Another explanation is that the refracture may have indeed be initiated in an orthogonal direction but as shown in figure 5.6(b), that the orthogonal refracture length may be too small for a tiltmeter to capture its orientation, bearing in mind that tiltmeter resolution degrades the farther its distance from the fracture. In field practice, tiltmeters are placed usually in a monitoring or offset well which are often several hundreds of feet away or at the surface (several thousands of feet from the fracture).

The deviation of field observation of initial refracture angle from the theoretical 90^o orientation may also be due to other factors such as the fracture bounding layer properties, crack toughness and natural fractures (discontinuities) in the medium [53].

Note that we have only considered the purely poroelastic case due to constant production rate (in an infinite medium) . While the extent of the 90^ore-orientation at the center of the crack, l_r is expected to change when mechanical effects (propped cracks) as well as constrained crack height are considered as discussed by Siebrits et al [53], it is however noteworthy that a plane strain approximation gave reasonably accurate results (for, l_r and the optimum time to refracture) compared to the bounded model in the mechanical-poroelastic case but with less computational requirements. The optimal time to refracture is when the stress reversal region around the fracture is maximum. The extent of the reversal however is dependent on the deviatoric stress in the medium prior to production. This in turn affects the optimal time to refracture the medium.

5.6 Conclusion

In this work, the stress re-orientation problem around an unpropped fractured producer well was revisited. A detailed mathematical formulation of the stress state and solutions were obtained in Laplace space and inverted back to time. The key contributions for this work are as follows:

The orthogonal segment of the theoretical refracture length, l_r profiles were generated as a function of time and dimensionless far-field deviator, $\mathcal{S}$. The refracture length profile as a function of $\mathcal{S}$ has not been previously reported in literature to the best of my knowledge.

Stress reorientation is observed even at very early times around the producer well for a

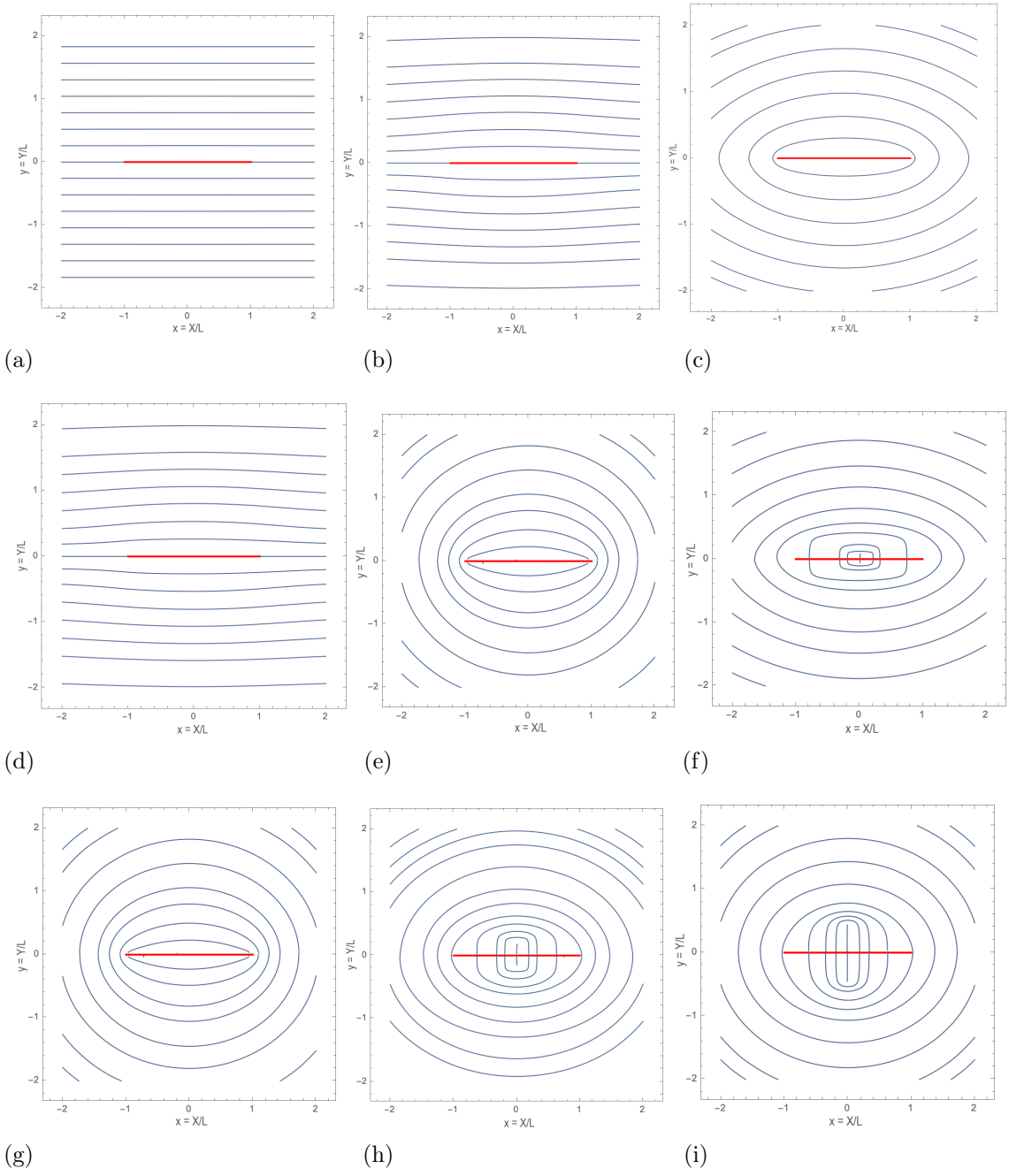

Figure 5.5: Stress trajectories around a fractured producer well at various $\mathcal{S}$ values at $\tau = 0.01, 1, 10$: (a) - (c) $\mathcal{S} = 0.35$ (d) - (f) $\mathcal{S} = 0.2$, (g) - (i) $\mathcal{S} = 0.1$

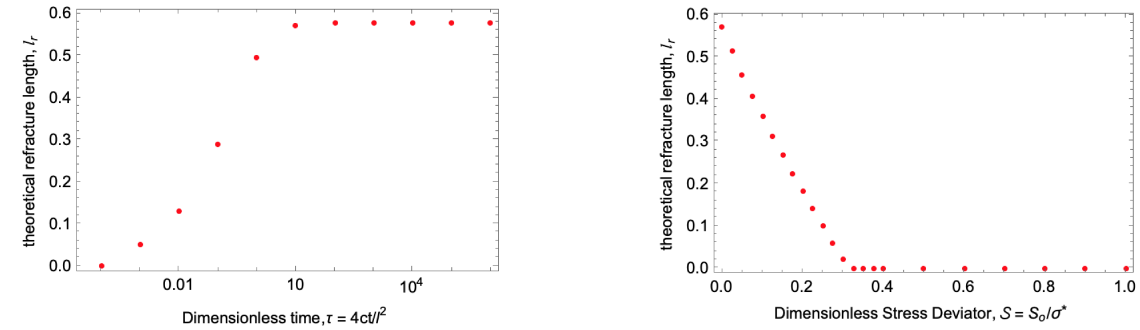

(a) (b)

Figure 5.6: Variation of the orthogonal segment of the theoretical refracture half-length,l_r with (a) τ at $\mathcal{S} = 0.01$ and (b) $\mathcal{S}$ at $\tau = 10$

medium with low initial far-field stress contrast. This is consistent with previous findings [45]. Such perturbation is however not observed if there exist a significant difference between the horizontal in-situ stresses.

For a medium with stress state close to being isotropic , the maximum orthogonal length of stress reversal region, l_r is 0.58 at $\tau \approx 10$ for a purely poroelastic consideration at constant production rate in an infinite medium. Again this is consistent with the findings by Siebrits et al [53]. The value of l_r however, decreases with increasing value of $\mathcal{S}$ even with increasing time of production. Other factors that could influence the value of l_r as noted by Siebrits et al [53] include fracture toughness and the properties of the bounding layers around the fracture.

The optimal time to refracture a producer well is when the stress reversal region around the fracture is maximum. The stress reversal region is however controlled by the stress deviator in the medium and as such different formations will have different optimal time to refracture.

For formations with significant stress deviator (non-isotropic stress state), the stress reversal region is significantly small. For a purely poroelastic infinite medium, for values of $\mathcal{S} \gtrsim 0.31$, there will be no stress reversal region, irrespective of the production time, however the stress field is still perturbed. This observation may perhaps be one of the several reasons there often exist a departure from the 90-degree refracture direction predicted by the refracture theory.

Chapter 6

Conclusions and Recommendations

6.1 Summary of Work and Contributions

This study examines two problems within the poroelastic framework.

The first problem focused on determining the induced stresses around an injector-producer pair and the possible path of propagation of a fracture initially equidistant between the two wells. Stress functions for quantifying the induced stresses were derived and stress trajectories were generated to describe the stress state around the wells. The major parameters influencing the potential path of propagation were highlighted and a new parameter was introduced into the stress trajectory equation to aid in estimating the fracture path without recourse to a full scale fracture propagation modeling.

The second problem considers a fractured producer and the potential path a refracture of such well will follow. This was studied using the stress trajectory equation after solving for the pore pressure and stress fields. The stress field re-orientation around the fractured producer and the conditions under which a complete reversal of the principal stress directions can occur was also studied. The major factors influencing the extent of an orthogonal refracture were identified. The profile of the refracture length as a function of time and dimensionless deviatoric stress were generated. The asymptotic expression for the dimensionless stress difference between the induced horizontal stresses at large times was also developed.

The major contributions of this study are as follows:

- For the Berchenko-Detournay problem, a new dimensionless toughness expression was suggested to approximate the effect of fracture toughness on the direction of a propagating fracture. The regular stress trajectory equation when modified with this expression gives approximate fracture propagation path even when the toughness is not small. The new expression makes it possible to use the stress trajectory to provide an estimate to the

fracture path without resorting to a full-fledged fracture propagation modeling.

- For the fractured producer well, a profile showing the variation of the theoretical refracture length with the dimensionless far-field stress deviator was developed. Such profile can provide a lower bound estimate of the expected orthogonal refracture length while planning a refracturing operation.

- A long-time asymptotic expression for the difference between the induced horizontal stresses was developed for the fractured well problem. This stress difference places a limit on the extent of the refracture length.

6.2 Recommendations

The following areas are suggested for further study

- The applicability of the new dimensionless toughness expression to other fracture propagation problems should be studied. Such study should also consider if this type of expression is problem specific or can be generalized. Extensive comparison between this adhoc approach to fracture path prediction and full scale numerical modeling for different propagation scenarios should be studied to determine its extent of application and limitations.

- The influence of proppants in the fracture should be studied as it will introduce mechanical effects into the induced stresses, stress reversal envelope and the theoretical refracture length. The variation of the refracture length with respect to time and the far field stress deviator should also be studied when proppants are present.

- A full scale numerical modeling of actual refracture path and the stress trajectory estimation should be considered for the fractured producer case. In addition, incorporating the modified dimensionless toughness expression and similar variants can be further explored to assess applicability.

Bibliography

[1] *Hydraulic Fracture Orientation and Production/Injection Induced Reservoir Stress Changes in Diatomite Waterfloods*, number SPE-29625-MS. Society of Petroleum Engineers (SPE), March 1995.

[2] J. I. Adachi. *Fluid-Driven Fracture in Permeable Rock*. PhD thesis, University of Minnesota, 2001.

[3] S. H. Advani, T. S. Lee, and J. K. Lee. Three dimensional modeling of hydraulic fractures in layered media: Finite element formulations. *ASME J. Energy Res. Tech.*, 112:1–18, 1990.

[4] Fathaddin M Aryanto A, Kasmungin S. (2018) hydraulic fracturing candidate-well selection using artificial intelligence approach. pages 1–7. Prosiding Seminar Nasional Cendekiawan., 2018.

[5] P.K. Banerjee, R. Butterfield, and G.R. Tomlin. Boundary element methods for two-dimensional problems of transient ground water flow. *Int. J. Numer. Anal. Methods Geomech.*, 5:15–31, 1981.

[6] Shook R.A Barba R.E. Post frac evaluation of multiple zone fracture treatments using the "completion efficiency" concept. spe annual technical conference and exhibition. society of petroleumengineers. Society of Petroleum Engineers, 2004.

[7] I. Berchenko and E. Detournay. Deviation of hydraulic fractures through poroelastic stress changes induced by fluid injection and pumping. *Int. J. Rock Mech. Min. Sci.*, 34(6):1009–1019, 1997.

[8] I. Berchenko, E. Detournay, and N. Chandler. Propagation of natural hydraulic fractures. *Int. J. Rock Mech. Min. Sci.*, 34(3-4):paper No. 063, 1997.

[9] M.A. Biot. General theory of three-dimensional consolidation. *J. Appl. Phys.*, 12:155–164, 1941.

[10] Maurice A Biot. General solutions of the equations of elasticity and consolidation for a porous material. *J. appl. Mech*, 23(1):91–96, 1956.

[11] M. Bouteca, J. Lessi, and J. P. Sarda. Stress changes induced by fluid injection in a porous layer around a wellbore. page 8, 1983.

[12] M.S. Bruno and F.M. Nakagawa. Pore pressure influence on tensile fracture propagation in sedimentary rock. *International Journal of Rock Mechanics and Mining Sciences & Geomechanics Abstracts*, 28(4):261 – 273, 1991.

[13] Andrew Bunger and Brice Lecampion. *Four Critical Issues for Successful Hydraulic Fracturing Applications*. Number Chapter 16. CRC Press, 2017.

[14] H. Carslaw and J. C. Jaeger. *Conduction of Heat in Solids*. Oxford University Press, 2nd edition, 1959.

[15] A.H.-D. Cheng and E. Detournay. On fundamental integral equations and fundamental solutions of poroelasticity. *Int. J. Solids Structures*, 35(34-35):4521–4555, 1998.

[16] Alexander H.-D. Cheng. *Poroelasticity*. Springer International Publishing, 2016.

[17] C. L. Cipolla and C. A. Wright. Diagnostic techniques to understand hydraulic fracturing: What? why? and how? 17:23–35, 2002.

[18] M. P. Cleary. Fundamental solutions for a fluid-saturated porous solid. *Int. J. Solids Structures*, 13:785–806, 1977.

[19] O. Coussy. *Mechanics of Porous Continua*. John Wiley & Sons., New York NY, 1995.

[20] Jeff Dahl, Philip Nguyen, Ron Dusterhoft, James Calvin, and Shameem Siddiqui. Application of micro-proppant to enhance well production in unconventional reservoirs: Laboratory and field results, 2015.

[21] E. Detournay and T.J Boone. Discussion of pore pressure influence on tensile fracture propagation in sedimentary rock. *Int. J. Rock Mech. Min. Sci. & Geomech. Abstr. & Geomech. Abstr*, 30(3):323–324, 1993.

[22] E. Detournay and A.H-D. Cheng. Plane strain analysis of a stationary hydraulic fracture in a poroelastic medium. *Int. J. Solids Structures*, 27(13):1645–1662, 1991.

[23] E. Detournay and Alexander H-D Cheng. 5 - fundamentals of poroelasticity. In Charles Fairhurst, editor, *Analysis and Design Methods*, pages 113 – 171. Pergamon, Oxford, 1993.

[24] Lawrence W. Teufel Dewi Triarti Hidayati, Her-Yuan Chen. Flow induced stress reorientation in a multiple well reservoir (spe 71091). 2001.

[25] Erle C. Donaldson, Waqi Alam, and Nasrin Begum. Field implementation of hydraulic fracturing, 2013.

[26] G. Dozier, J. Elbel, E. Fielder, R. Hoover, S. Lemp, S. Reeves, E. Siebrits, D. Wisler, and S. Wolhart. Refracturing works. *Oilfield Review*, pages 38–53.

[27] M.J. Economides and K.G. Nolte. *Reservoir Stimulation*. Wiley, 3rd edition, 2000.

[28] J.L. Elbel and M.G. Mack. Refracturing: Observations and theories (SPE 25464). In *Proc. Production Operation Symposium*, pages 521–531, Richardson, Texas, 1993. SPE.

[29] F. FragachÃ¡n, M. P. Shahri, D. Arnold, A. Babey, and C. Smith. Enhancingwell performance via in-stage diversion in unconventional wells:physics and case studies. *SPE Argentina exploration and production of unconventional resources symposium. Society of PetroleumEngineers*, 2016.

[30] J. Geertsma. A remark on the analogy between theromoelasticity and the elasticity of saturated porous media. *J. Mech. Phys. Solids*, 6:13–16, 1957.

[31] Ahmad Ghassemi. *Three-dimensional poroelastic hydraulic fracture simulation using the displacement discontinuity method*. PhD thesis, University of Oklahoma, 1996.

[32] Bill Grieser, James Calvin, and James Dulin. Lessons learned: Refracs from 1980 to present. 2016.

[33] Sharma Abhishek Gupta, Supriya and Aria Abubakar. Artificial intelligence–driven asset optimizer. SPE Annual Technical Conference and Exhibition, September 2018.

[34] Ebrahim Fathi Hoss Belyadi and Fatemeh Belyadi. *Hydraulic Fracturing in Unconventional Reservoirs*. Gulf Professional Publishing, 2019.

[35] M.K. Hubert. Mechanics of hydraulic fracturing. *Petroleum Trans., AIME*, 210:153–168, 1957.

[36] Tsuyoshi Ishida, Qu Chen, Yoshiaki Mizuta, and Jean-Claude Roegiers. Influence of fluid viscosity on the hydraulic fracturing mechanism. 126:190–200, 2004.

[37] Trent Jacobs. Changing the equation: Refracturing shale oil wells. *Journal of Petroleum Technology*, 67 (04)(Paper Number: SPE-0415-0044-JPT):44–49., April 2015.

[38] Trent Jacobs. Shale refracs: Next big thing, or a piece of the big puzzle? *Journal of Petroleum Technology*, 74 (11)(Paper Number: SPE-1122-0018-JPT):18–26., November 2022.

[39] Rhodine C.N Jacquot R.G, Steadman J.W. The gaver-stehfest algorithm for approximate inversion of laplace transform. *in IEEE Circuits and Systems Magazine*, 5(1):4–8, March 1983.

[40] John T Katsikadelis. *Boundary elements: theory and applications*. Elsevier, 2002.

[41] Lingyun Kong, Mehdi Ostadhassan, Naser Tamimi, Shirin Samani, and Chunxiao Li. Re-fracturing: well selection, treatment design, and lessons learned - a review. 12, 2019.

[42] W. A. Minner, C. A. Wright, G. R. Stanley, C. J. de Pater, T. L. Gorham, L. D. Eckerfield, and K. A. Hejl. Waterflood and production-induced stress changes dramatically affect hydraulic fracture behavior in lost hills infill wells. page 13, 2002.

[43] Hai T. Nguyen, Jang Hyun Lee, and Khaled A. Elraies. A review of pkn-type modeling of hydraulic fractures. 195:107607, 2020.

[44] J. L. Reese, L. K. Britt, and J. R. Jones. Selecting economic refracturing candidates. New Orleans, Louisiana,, September 1994. Paper presented at the SPE Annual Technical Conference and Exhibition.

[45] Nicolas P. Roussel and Mukul M. Sharma. Role of stress reorientation in the success of refracture treatments in tight gas sands. *SPE Production & Operations*, 27(04):346–355, 2012.

[46] Nicolas P. Roussel and Mukul M. Sharma. Selecting candidate wells for refracturing using production data. *SPE Production and Operations*, 28:36–45, 2013.

[47] E. Sarvaramini and D. I. Garagash. Breakdown of a pressurized finger-like crack in a permeable rock. *J. Appl. Mech.*, 82(6):061006, 2015.

[48] E. Sarvaramini and D. I. Garagash. Poroelastic effects on reactivation of a fingerlike hydraulic fracture. *J. Appl. Mech.*, 83:061001, 2016.

[49] Arash Shadravan, Mohammadali Tarrahi, and Mahmood Amani. Intelligent tool to design fracturing, drilling, spacer and cement slurry fluids using machine learning algorithms, 2015.

[50] Maunish Shah, Jatin R. Agarwal, Dipal Patel, Jaydeepkumar Chauhan, Dhruvin Kaneria, and Subhash N. Shah. An assessment of chemical particulate technology as diverters for refracturing treatment. 84:103640, 2020.

[51] Maunish Shah, Subhash Shah, and Anirbid Sircar. A comprehensive overview on recent developments in refracturing technique for shale gas reservoirs. *Journal of Natural Gas Science and Engineering*, 46:350–364, 2017.

[52] E. Siebrits, J. L. Elbel, R. S. Hoover, I. R. Diyashev, L. G. Griffin, S. L. Demetrius, C. A. Wright, B. M. Davidson, N. P. Steinsberger, and D. G. Hill. Refracture reorientation enhances gas production in barnett shale tight gas wells. page 7, 2000.

[53] E. Siebrits, J.L. Elbel, E. Detournay, C. Detournay-Piette, M. Christianson, B.M. Robinson, and I.R. Diyashev. Parameters affecting azimuth and length of a secondary fracture during a refracture treatment (SPE 48928). In *Proc. SPE Annual Technical Conference and Exhibition*, pages 17–27, Richardson, Texas, 1998. SPE.

[54] Shekhar Sinha and Hariharan Ramakrishnan. A novel screening method for selection of horizontal refracturing candidates in shale gas reservoirs. paper presented at the north american unconventional gas conference and exhibition, the woodlands, texas, usa. June 2011.

[55] I. N. Sneddon and H. A. Elliot. The opening of a Griffith crack under internal pressure. *Quarterly of Applied Mathematics*, 4:262–267, 1946.

[56] H. Stehfest. Numerical inversion of laplace transform. *Communications of the ACM*, 13, 1970.

[57] L. Vandamme, E. Detournay, and A.H-D. Cheng. A two-dimensional poroelastic displacement discontinuity method for hydraulic fracture simulation. *Int. J. Numer. Anal. Methods Geomech.*, 13:215–224, 1989.

[58] M. C. Vincent. Refracs: Why do they work, and why do they fail in 100 published field studies? Paper presented at the SPE Annual Technical Conference and Exhibition, September 19–22, 2010 Paper Number: SPE-134330-MS, Society of Petroleum Engineers, 2010.

[59] Dao-Bing Wang, Fu-Jian Zhou, Yi-Peng Li, Bo Yu, Dmitriy Martyushev, Xiong-Fei Liu, Meng Wang, Chun-Ming He, Dong-Xu Han, and Dong-Liang Sun. Numerical simulation of fracture propagation in russia carbonate reservoirs during refracturing. *Petroleum Science*, 19:2781 – 2795, May 2022.

[60] Herbert F. Wang. *Theory of Linear Poroelasticity with Applications to Geomechanics and Hydrogeology*. Princeton University Press, 2000.

[61] Sharon Yunhong Wang, Xin Lucy Luo, and Robert Samuel Hurt. What we learned from a study of re-fracturing in barnett shale: An investigation of completion/fracturing, and production of re-fractured wells, 2013.

[62] Norman R. Warpinski and Paul T. Branagan. Altered-stress fracturing. *Journal of Petroleum Technology*, 41(09):990–997, 1989.

[63] C. A. Wright, R. A. Conant, D. W. Stewart, and P. M. Byerly. Reorientation of propped refracture treatments. In *Proc. EuRock'94, SPE/ISRM Rock Mechanics in Petroleum Engineering*, pages 417–424. Balkema, 1994.

[64] Yu-Shu Wu. Hydraulic fracture modeling, 2017.

[65] Derek Elsworth Xiang Li, Jiehao Wang. Stress redistribution and fracture propagation during restimulation of gas shale reservoirs. *Journal of Petroleum Science and Engineering*, 154:150 – 160, June 2017.

[66] Yunxin Xie, Chenyang Zhu, Wen Zhou, Zhongdong Li, Xuan Liu, and Mei Tu. Evaluation of machine learning methods for formation lithology identification: A comparison of tuning processes and model performances. 160:182–193, 2018.

[67] Jiaher Tian Zhijie Huang. Method for refracturing a wellbore and low molecular weight composition for use therein, July 2019.

Appendix A: Poroelastic Constants

The expressions for the the poroelastic constants described in chapter 3 are provided below

$$v = \frac{3K - 2G}{2(3K + G)} \tag{1}$$

$$v_u = \frac{3K_u - 2G}{2(3K_u + G)} \tag{2}$$

$$B = \frac{3(v_u - \nu)}{\alpha(1 - 2v)(1 + v_u)} \tag{3}$$

$$M = \frac{2G(v_u - v)}{\alpha^2(1 - 2v_u)(1 - 2v)} \tag{4}$$

$$\eta = \frac{\alpha(1 - 2v)}{2(1 - v)} \tag{5}$$

$$S = \frac{(1 - v_u)(1 - 2\nu)}{M(1 - v)(1 - 2v_u)} \tag{6}$$

Appendix B

B.1 Numerical Solution to Auxiliary problem

I have adopted the Boundary Element Method approach to solve the integral equation ((5.8)) . First we rewrite the equation in approximate form by discretizing the straight fracture into N boundary elements or segments ($N = 100$ in the code), using $N + 1$ Chebyshev nodes. Source densities are distributed and collocated at the mid-point of each element. Also, the source densities are taken to be constant on each element.

Equation ((5.8)) can be written in its discretized form as

$$-\frac{1}{s} = \frac{2}{\pi} \sum_{j=1}^{N} \overset{ij}{G} \psi(\overset{j}{x'}, s) \tag{7}$$

Where $\overset{ij}{G}$ is the influence coefficient matrix given by

$$\overset{ij}{G} = \int_{\Gamma_j} K_o \left(2\sqrt{s} |\xi_i - \xi_j^{'}| \right) d\Gamma \tag{8}$$

and

$$d\Gamma = \frac{l_j}{2} d\varepsilon \tag{9}$$

l_j is the length of element j.

The values for the integral expression (8) for the coefficient matrix is obtained using the standard Gaussian quadrature scheme. The Gaussian integration is performed over the interval $-1 \leq \xi^{'} \leq 1$.

Given a function$f(\varepsilon)$ to be integrated over the interval $-1 \leq \epsilon \leq 1$, we can write

$$\int_{-1}^{1} f(\varepsilon) d\varepsilon \approx \sum_{k=1}^{n} w_k f(\varepsilon_k) \tag{10}$$

where n is the number of integration points (Gauss points), w_k and ε_k are the weights and abscissas of the Gaussian quadrature of order $n = 10$ (in the code). Consider an element j over which the integration will be carried out. Its endpoints in a global coordinate system (ξ, η) with origin $(0, 0)$ are described by (ξ_j, η_j) and (ξ_{j+1}, η_{j+1}). We can relate the global coordinates onto a local system of coordinate $(\varepsilon, 0)$, on the integration interval, $[-1, +1]$ using the following coordinate transformation:

$$\xi^{'}(\varepsilon) = \frac{\xi_{j+1}^{'} + \xi_j^{'}}{2} + \frac{\xi_{j+1}^{'} - \xi_j^{'}}{l_j} \varepsilon \tag{11}$$

$$\eta^{'}(\varepsilon) = \frac{\eta^{'}_{j+1} + \eta^{'}_{j}}{2} + \frac{\eta^{'}_{j+1} - \eta^{'}_{j}}{l_j}\varepsilon, \tag{12}$$

Where

$$l_j = \sqrt{(\xi'(\varepsilon_k) - \xi'_j)^2 + (\eta(\varepsilon_k) - \eta_j)^2} \tag{13}$$

is the length of element j.

Equation (8) produces a $N \times N$ matrices upon discretization. $\psi(\overset{j}{x'}, s)$are vectors of dimension N. While system of $N|$ linear algebraic equations are produced with N number of unknowns which can be solved to recover $\psi(x', s)$.

B.2 Auxiliary Induced Stresses

The components of the induced stresses due to the auxiliary problem in equation (5.20) are given as follows:

$$\hat{\sigma}^{aux}_{yy}(x, y, s) = \frac{1}{\pi}\int_{-1}^{1} \frac{\psi^{aux}(x^{'}, s)}{sr^2}\left[\frac{(x-x')^2 - y^2}{r^2} - 4s(x-x')^2 K_0(2\sqrt{sr^2})\right.$$

$$\left. - \frac{2((x-x')^2 - y^2)\sqrt{sr^2}K_1\left(2\sqrt{sr^2}\right)}{r^2}\right] dx' \tag{14}$$

$$\hat{\sigma}^{aux}_{xx}(x, y, s) = \frac{1}{\pi}\int_{-1}^{1} \frac{\psi^{aux}(x^{'}, s)}{sr^2}\left[\frac{y^2 - (x-x')^2}{r^2} - 4sy^2 K_0(2\sqrt{sr^2})\right.$$

$$\left. - \frac{2(y^2 - (x-x')^2)\sqrt{sr^2}K_1\left(2\sqrt{sr^2}\right)}{r^2}\right] dx' \tag{15}$$

$$\hat{\sigma}^{aux}_{xy}(x, y, s) = \frac{1}{\pi}\int_{-1}^{1} \frac{\psi^{aux}(x^{'}, s)}{sr^2}\left[-2\frac{y(x-x')}{r^2} + 4sy(x-x')K_0(2\sqrt{sr^2})\right.$$

$$\left. + \frac{4(y(x-x'))\sqrt{sr^2}K_1\left(2\sqrt{sr^2}\right)}{r^2}\right] dx' \tag{16}$$

$$\hat{\Pi}(s) = \frac{1}{\pi s}\left(ln\left(\frac{s}{4}\right) + 2\gamma\right) \tag{17}$$

Where $r = \sqrt{(x-x^{'})^2 + y^2}$

B.3Asymptotic Induced deviatoric Stress Derivation

The induced stresses due to constant rate of production is given by

$$\sigma_{ij}^{ind}(x,y,t) = \int_0^t \sigma_{ij}^{aux}(x,y,t-t^{'})\frac{dp}{dt'}dt' \tag{18}$$

Taking Laplace transform of (18), we get

$$\hat{\bar{\sigma}}_{ij}^{ind}(x,y,s) = \hat{\sigma}_{ij}^{aux}(x,y,s)s\hat{\Pi}(s) \tag{19}$$

where the components of $\hat{\sigma}_{ij}^{aux}(x,y,s)$ are provided in Appendix B.2

The large time expression for the leak in rate $\psi^{aux}(x^{'},s)$ for the auxiliary problem has been provided by Sarvaramini and Garagash [47] as

$$\psi^{aux}(x^{'},s) = -\frac{1}{\sqrt{1-x'^2}}\frac{1}{s(ln(s/4)+2\gamma)} \tag{20}$$

and $r = \sqrt{(x-x^{'})^2+y^2}$

Using the Asymptotic expressions for the modified Bessel functions for small argument $z = 2\sqrt{sr^2}$

$$K_0(z) = -\gamma + ln(2/z) \tag{21}$$

and

$$K_1 = \frac{1}{z} + \frac{z}{4}\left(-1+2\gamma-2ln(2/z)\right) \tag{22}$$

Along the crack plane, $y = 0$

Thus, substituting (20), (21) and (22) into equations (14) - (16), we obtain the asymptotic expressions for the auxiliary induced stresses along the crack as

$$\hat{\sigma}_{xx,asym}^{aux}(x,s) = \frac{1}{2s(ln(s/4)+2\gamma)}\left(-2+4\gamma+ln\left(s(x-1)^2\right)+ln\left(s(x+1)^2\right)\right) \tag{23}$$

$$\hat{\sigma}_{yy,asym}^{aux}(x,s) = \frac{1}{2s(ln(s/4)+2\gamma)}\left(2+4\gamma+ln\left(s(x-1)^2\right)+ln\left(s(x+1)^2\right)\right) \tag{24}$$

$$\hat{\sigma}_{xy,asym}^{aux}(x,s) = 0 \tag{25}$$

Thus, the asymptotic expressions for the induced stresses along the crack due to continuous production is obtained by substituting (23), (23) and (24) into (19).

$$\hat{\sigma}_{xx,asym}^{ind}(x,s) = \frac{1}{2\pi s}\left(-2+4\gamma+ln\left(s(x-1)^2\right)+ln\left(s(x+1)^2\right)\right) \tag{26}$$

$$\hat{\sigma}^{ind}_{yy,asym}(x,s) = \frac{1}{2\pi s}\left(2 + 4\gamma + ln\left(s(x-1)^2\right) + ln\left(s(x+1)^2\right)\right) \tag{27}$$

Thus, the asymptotic induced deviatoric stress along the crack is

$$\Delta\sigma = \hat{\sigma}^{ind}_{xx,asym}(x,s) - \hat{\sigma}^{ind}_{yy,asym}(x,s)) \tag{28}$$

$$\Delta\sigma = -\frac{2}{\pi s} \tag{29}$$

Inverting (29) back to time domain gives

$$\Delta\sigma = -\frac{2}{\pi} \approx -0.6366 \tag{30}$$